ISTANBUL TECHNICAL UNIVERSITY ★ GRADUATE SCHOOL

HEAT TRANSFER AND FLOW ANALYSIS IN A SPIRAL CHANNEL FILLED WITH STEEL BALLS

M.Sc. THESIS

Ali AMIRFARIDI

Department of Mechanical Engineering

Thermo Fluids Programme

FEBRUARY 2023

ISTANBUL TECHNICAL UNIVERSITY ★ GRADUATE SCHOOL

HEAT TRANSFER AND FLOW ANALYSIS IN A SPIRAL CHANNEL FILLED WITH STEEL BALLS

M.Sc. THESIS

Ali AMIRFARIDI
(503191103)

Department of Mechanical Engineering

Thermo Fluids Programme

Thesis Advisor: Prof. Dr. Mustafa ÖZDEMİR

FEBRUARY 2023

ISTANBUL TEKNİK ÜNİVERSİTESİ ★ LİSANSÜSTÜ EĞİTİM ENSTİTÜSÜ

SPİRAL KANAL İÇERİSİNE BİLYE YERLEŞTİRİLEREK OLUŞTURULAN GÖZENEKLİ ORTAMLARDA AKIŞ VE ISI GEÇİŞİ ANALİZİ

YÜKSEK LİSANS TEZİ

Alı AMIRFARIDI
(503191103)

Makine Mühendisliği Anabilim Dalı

Isı Akışkan Programı

Tez Danışmanı: Prof. Dr. Mustafa ÖZDEMİR

ŞUBAT 2023

Ali AMIRFARIDI, a M.Sc. student of İTU Graduate School student ID 503191103, successfully defended the thesis entitled "**HEAT TRANSFER AND FLOW ANALYSIS IN A SPIRAL CHANNEL FILLED WITH STEEL BALLS**", which he prepared after fulfilling the requirements specified in the associated legislations, before the jury whose signatures are below.

Thesis Advisor :	**Prof. Dr. Mustafa ÖZDEMİR** İstanbul Technical University	....
Jury Members :	**Prof. Dr. Lütfullah Kuddusi** Istanbul Technical University	....
	Prof. Dr. Ş. Özgür Atayılmaz Yildiz Teknik University	....

Date of Submission : 30 December 2022
Date of Defense : 2 February 2023

To my family,

FOREWORD

I would like to thank my parents, Mina and Farrokh, my sister Tannaz, and my uncle Farzin, whom without their support and vision I would not be able to come this far and past that border in the first place. My deepest appreciation to my dear wife, Idil, that during the time I was writing this thesis, show great patience and support. And thanks to my best friends, Oğuz and Cansu, whom their presence and companionship along the years made a foreign country home.

My most sincere gratitude to my advisor, Prof. Dr. Mustafa Özdemir, who lit the way with knowledge for me through dark times of pandemic and believed in me until the last moment. His studies in the field of heat transfer in porous media was a breakthrough that enlightened me, and his advisory along this period helped me achieve the results to base this thesis on.

December 2022

Ali AMIRFARIDI
(Mechanical Engineer)

TABLE OF CONTENTS

Page

ABBREVIATIONS

REV **:** Representative Elementary Volume
LTE **:** Local Thermal Equilibrium
BC **:** Boundary Condition
IC **:** Initial Condition

SYMBOLS

V	**:** Velocity Vector
ρ	**:** Density $[kg/m^3]$
$\boldsymbol{\rho_f}$	: Fluid Density $[kg/m^3]$
Um	**:** Mean Velocity $[m/s]$
$\boldsymbol{\varepsilon}$	: Porosity
$\boldsymbol{V}$	: Volume $[m^3]$
$\boldsymbol{V_f}$	: Volume of the Fluid-phase $[m^3]$
$\boldsymbol{V_s}$	: Volume of the Solid phase $[m^3]$
L	: Linear Dimension of the System $[m]$
$\boldsymbol{\ell}$	: Representative Elementary Volume Length $[m]$
K	: Permeability $[m^2]$
$\boldsymbol{d_p}$	: Particle diameter $[m]$
$\boldsymbol{\mu_f}$	: Fluid Viscosity $[Pa-s]$
$\mathbf{Re_K}$	: Permeability based Reynolds Number
$\boldsymbol{u_f}$	: Fluid-phase velocity $[m/s]$
$\boldsymbol{u_m}$	: Seepage Velocity $[m/s]$
$\boldsymbol{h(r)}$	: Local flows depth at radial distance $[m]$
$\boldsymbol{r}$	: Radius $[m]$
$\boldsymbol{\theta}$	: Curvature direction of channel
z	: Channel height-wise direction
$\boldsymbol{u_r}$	: velocity in r-direction $[m/s]$
$\boldsymbol{u_\theta}$	: velocity in θ-direction $[m/s]$
$\boldsymbol{u_z}$	: velocity in z-direction $[m/s]$
$\boldsymbol{\psi}$	: any scalar quantity
$\boldsymbol{A}$	: Area $[m^2]$
$\boldsymbol{A_f}$	: Area of fluid-phase $[m^2]$
$\Delta\boldsymbol{d}$	: A specific control element
$\boldsymbol{t}$	: Time $[s]$
$\boldsymbol{\vec{\imath}_r}$	: Unit vector in r-direction

$\vec{\iota_\varphi}$	: unit vector in φ-direction
$\vec{\iota_z}$	: unit vector in z-direction
$\boldsymbol{u}$	: velocity in r-direction $[m/s]$
$\boldsymbol{v}$	: velocity in φ-direction $[m/s]$
$\boldsymbol{w}$	: velocity in z-direction $[m/s]$
$\boldsymbol{\varphi}$	: angle and curvature direction into channel $[rad]$
$\boldsymbol{P}$	: Pressure $[Pa]$
$\boldsymbol{\mu}$	: Viscosity $[Pa-s]$
$\boldsymbol{k}$	: Thermal Conductivity $[W/m-K]$
$\boldsymbol{T}$	: Temperature $[K]$
$\boldsymbol{R}$	: Spiral radii $[m]$
$\boldsymbol{R_{min}}$	: Minimum radius of spiral $[m]$
$\boldsymbol{c}$	: Channel pitch $[mm]$
$\boldsymbol{C_\varphi}$	: Pressure drop in φ-direction
$\boldsymbol{r_m}$	: radius in middle of the cylindrical channel $[m]$
$\boldsymbol{r_i}$	: Inner wall radius of the cylindrical channel $[m]$
$\boldsymbol{r_o}$	: Outer wall radius of the cylindrical channel $[m]$
$\boldsymbol{H}$	: Channel height $[m]$
$\boldsymbol{k_f}$	: Fluid-phase thermal conductivity $[W/m-K]$
$\boldsymbol{k_s}$	: Solid-phase thermal conductivity $[W/m-K]$
$\boldsymbol{k_{eff}}$	: Effective thermal conductivity $[W/m-K]$
$\boldsymbol{k_d}$	: Dispersion thermal conductivity $[W/m-K]$
$\boldsymbol{k_{tot}}$	: Total thermal conductivity $[W/m-K]$
$\boldsymbol{C_{p,f}}$	: Specific heat of the fluid at constant pressure $[J/kg-K]$
$\boldsymbol{C_T}$	: Temperature change coefficient in φ-direction $[K/rad]$
$\boldsymbol{T_{in}}$	: Fluid temperature at channel inlet $[K]$
$\boldsymbol{q}$"	: Heat Flux applied on the walls $[W/m^2]$
$\dot{\boldsymbol{m}}$	: Flow rate $[g/s]$
d	: Channel width $[m]$
$\boldsymbol{Re_{dh}}$	: Hydrodynamic diameter-based Reynold’s number

LIST OF TABLES

LIST OF FIGURES

Page

HEAT TRANSFER AND FLOW ANALYSIS IN A SPIRAL CHANNEL FILLED WITH STEEL BALLS

SUMMARY

Flow through porous medium, still fascinates curious minds of researchers with many unknown properties, and characteristics ready to be discovered. Hydrodynamical effects within the flow, and corresponding heat transfer outcomes, all create impacts which assist the enhancement in thermal properties of the porous system.

In this study, a flow in spiral channel filled with AISI 1010 steel balls is studied based on experimental results of Gokaslan et al. (2022), under different flow rates, considering a constant wall heat flux boundary condition through side walls of the channel. The aim of the study was to create analytical solutions and create a simulation using COMSOL Multiphysics software in order to study thermal dispersion values using results obtained from experimental data and analytical solutions.

While processing the analytical solutions, due to complex geometry of the experimental system (Arithmetic spiral), some assumptions have been made in order to simplify, and obtain analytical solutions for the system. Therefore, both momentum and energy equations for the system are solved using cylindrical coordinates due to low curvature ratio, considering an incompressible, steady state fully developed flow.

Finally, as a contribution to literature, in order to make analytical solutions independent of values derived from experimental results and overcome this constraint, which these values were used as boundary conditions to obtain a valid solution, a correlation-based equation for temperature distribution along the channel, according to fluid properties such as viscosity, thermal conductivity and inlet flow rate, besides channel and system properties of applied heat flux, utilized steel balls diameter and channel width, was obtained.

Both analytical solutions and the correlation-based equations show good agreement with experimental results, and their error for temperature distribution values has been at a maximum value of %6.1 which can be considered accurate.

Furthermore, the coefficients used in correlation-based equation have only an error value of %5.35 considering same coefficients derived from experimental results.

SPİRAL KANAL İÇERİSİNE BİLYE YERLEŞTİRİLEREK OLUŞTURULAN GÖZENEKLİ ORTAMLARDA AKIŞ VE ISI GEÇİŞİ ANALİZİ

ÖZET

Spiral kanallardaki akışlar, hem doğadaki varlıkları, hemde akış ve ısı transferinde oluşturabildikleri çok sayıda etkilerinden dolayı hep merak edilip, bilim insanlarının ilgi odağı olmuşlardır. Bu alanda uzun yıllardan beri çok sayıda çalışma mevcuttur. Gözenekli ortamda da ise, ısı transferinin daha farklı sebeplerden, örneğin yüzey alanı artmasından dolayı, arttığını gözlemlemekteyiz. İki özelliğin aynı anda kullanılması halinde, daha verimli ve iyi sonuçlar alınması beklenmesine rağmen, konu ile ilgili yeterli araştırma bulunmamaktadır.

Çalışmamızda, çelik bilyelerle gözenekli ortamı oluşturulmuş spiral bir kanalda, hem momentum, hemde enerji korunumu denklemleri olmak üzere, bir sayısal çözüm arayışı ve aynı zamanda COMSOL yazılımını kullanarak en uygun simülasyon oluşturularak, ısıl dispersiyon kat sayısının analizi hedeflenmiştir.

Analitik Çözüm

Bu çalışmada elde edilen sayısal sonuçlar, belirli varsayımlar kullanarak (tam gelişmiş ve sıkıştırılamaz akış, zamandan bağımsız), ve spiral kanal geometrisinin oluşturduğu komplikasyonlar düşünülerek, silindirik koordinatlarda çözülmüş olup, çıkan sonuçları deneysel sonuçlarda çıkan verilerle kanal boyu uyuşmaktadır. Bu yöntem ile elde edilen değerleri kullanmak için ihtiyaç duyulan dispersiyon iletkenlik kat sayısı (k_d) tum akışlar değerleri için hesaplanıp, elde edilen değerlerin ortalaması olarak 3.07 $[W/m\ K]$ tum hesaplamalarda kullanılmıştır.

Analitik çözüm ve deneysel sonuçlar arasındaki tek farklılık durumu ise, analitik çözüm oluşturulurken kanal sonundaki ısıl kayıplar baz alınmadığından dolayı, kanal çıkış sıcaklıkları arasında farklılıklar bulunmaktadır. Bu durum göz önünde bulundurularak, sayısal çözümün hata payı ve dikkat oranı, sadece 270 dereceye kadar olan deneysel verilerle kıyaslanıp değerlendirilmiştir.

Elde edilen analitik çözüm, silindirik koordinatlarda tam gelişmiş sürekli bir akış için, denklem (0.2) de verilmiştir. Bu denklem, başlangıç ve sınır şartlarından dolayı deneysel sonuçlara bağlantılı olup, elde edilen değerlerde en çok etkiye sahip olan C_T kat sayısı, deneysel sonuçlardaki kanal boyu sıcaklık değişikliklerinden elde edilmektedir. Bu çözümde kullanılan J kat sayısı ise, denklem (0.1) de sunulmuştur.

$$J = \frac{-\rho_f C_{p,f} K C_\varphi C_T}{k_{tot}\ \mu_f} \tag{0.1}$$

$$\langle T\rangle(r,\varphi) = \frac{J}{2}.\,ln^2\left(\frac{r_m}{r}\right) + \frac{q"r_m}{k_{tot}}.\,ln\left(\frac{r_m}{r}\right) + C_T.\,\varphi + T_{in} \tag{0.2}$$

COMSOL Multiphysics Simülasyonu

COMSOL yazılımı kullanılarak gerçekleştirilen simülasyon sonucundaki çözümü ise, kanal çıkışındaki ışıl kayıplarını hesaba katması sonucu, çıkış sıcaklıklarına çok yakın değerler elde etmiş olup, ancak kanal boyu gerçekleşen sıcaklık artışını doğru oranda yansıtamamıştır.

Korelasyona Dayalı Çözüm

Bu iki yönteme ek olarak, sayısal çözümdeki hesaplamalarda, doğru çözümü bulmak için kullanılan sınır şartlarından dolayı, sayısal çözümlerde deneysel veriler ve sonuçlara bağlı olmak zorunda kalıyoruz. Bu kısıtı aşmak, ve sadece akışın girişteki değerlerini kullanarak kanal boyu bir sıcaklık değişimi öngörüsünde bulunabilmek için, korelasyona dayalı kanal içerisindeki sıcaklık değişimi için bir denklem geliştirildi. Bu denklem, hidrolik çap dayalı Reynolds sayısına bağlıdır ve bu değerin 1500 altı ve üstü koşuluyla, katsayıları farklılık gösteriyordur.

Bu yöntem ile elde edilen sonuçlar, hidrolik çap dayalı Reynolds değeri 1500 ve üzeri olan akışlarda, kanal boyunca deneysel sonuçlara en yakın değerleri vermişlerdir. Sonuçlardaki hata oranı ise, hidrolik çap dayalı Reynolds değerinin azalması ile yükselmektedir. Korelasyona dayalı kanal içerisindeki sıcaklık değişimi, denklem (0.3) kullanılarak hesaplanabilmektedir. Bu denklemde kullanılan a ve b kat sayılarının değerleri, her iki hidrolik çap dayalı Reynolds değerine göre denklem (0.4) ve (0.5)'te sunulmuştur.

Bu denklem sayesinde, deneysel sonuçlardan bağımsız ve uygulanan başlangıç şartlarına dayalı kanal boyu doğru sonuçlar elde etme imkânı vardır. Kullanılan başlangıç değerleri ise, uygulanan ısı akışı, akış debisi, akışkanın ısıl iletkenlik kat sayısı ve viskozitesi, kullanılan bilye çapı ve silindirik kanalın çapıdır.

$$\langle T\rangle(r,\varphi) = \frac{J}{2}.\,ln^2\left(\frac{r_m}{r}\right) + \frac{q"r_m}{k_{tot}}.\,ln\left(\frac{r_m}{r}\right) + \left(\frac{a\,q"\,\mu_f}{\dot{m}\,k_f\,\pi}\left(\frac{d_p}{d}\right)^b\right).\,\varphi + T_{in} \tag{0.3}$$

$$a = 1.6379\,, b = 0.98463 \qquad \boldsymbol{Re_{dh} \geq 1500} \tag{0.4}$$

$$a = 0.3424\,, b = 0.05313 \qquad \boldsymbol{Re_{dh} < 1500} \tag{0.5}$$

Sonuç ve Değerlendirme

Her üç yöntem (sayısal, korelasyona dayalı ve COMSOL üzerindeki simülasyon) ile elde edilen sonuçlar, daha önce gerçekleştirilmiş olan deney sonuçlarıyla kıyaslanıp, hata payları ölçülmüştür. Analitik çözümün sonuçlarında, deneysel sonuçlara kıyasen kanal boyu sıcaklık değişimindeki maksimum hata payı %6.1 olmuştur. Bu hata payı oranı, akış debisi artışıyla beraber azalmakta olup, en düşük değeri denenmiş olan en yüksek akış debisinde elde edilmiş olup, %6.1 hata payı ise, denenmiş olan en küçük debi değerinde elde edilmiştir.

1. INTRODUCTION

Heat transfer enhancement is a critical issue that directly affects a wide range of industries and engineering fields, including cooling and heating applications, solar receivers, chemical and nuclear reactors etc. Further developments of this field, imposes vital impact on global energy crisis and can play an important role on various solutions for this matter, such as waste heat recovery, which is a major topic in this field and one of the focus points of corresponding international projects and researches such as European Horizon Projects.

Numerous methods are utilized along history in order to contribute and enhance the heat transfer ratio. Applying fins, using various porous medium, changing the channel properties and flow geometry are just some of the basic methods known as passive methods which have been preferred and been subject of the studies, since they neither do require additional equipment, nor increase the complexity and capital of the system in comparison to the active systems, they are widely used in process industries.

As a result of such studies and applications, it is known that utilizing a curved channel or applying porous medium into the channels may enhance heat transfer. There are different parameters which have direct impact on the possible enhancement. Curvature ratio, channel width and channel geometry are examples of the parameters influential in curved channels, while type of the porous medium, utilized material, porosity etc. are basic known parameters of the latter method. Despite vast studies existing on these matters separately, there are few studies combining the two methods. In both cases of applying porous medium or using curved channels, occurrence of secondary flows and existence of turbulence improves heat transfer correspondingly; especially spiral channels provide more promising results in comparison to other curved channels.

This study provides analytical solutions for a spiral heat exchanger applied on cylindrical coordinates, a correlation-based equation for temperature estimations in spiral packed beds with the same properties, followed by verification of the analytically obtained results by a COMSOL based computer simulation and experimental data.

Conservation of mass, momentum and energy equations are solved based on the assumptions provided in Chapter 2, besides corresponding correlation is presented. COMSOL based results and details of the simulation are presented in Chapter 3 and the verification of the results within the methods of the former chapters are done against experimental data obtained by Gokaslan et al. (2022) in Chapter 4.

1.1 Purpose of Thesis

As formerly mentioned, literature lacks studies containing both spiral channels with applied porous medium. Since the occurring turbulence due to the applied porous medium and spiral channel geometry, is a matter enhancing the heat transfer while separately utilized, therefore it is expected to observe better enhancement by combining curved channels and applying porous medium together.

This study focuses on providing analytical solution to the conservation equations of this type based on cylindrical coordinates while using the volume averaging method, REV and LTE assumption. Furthermore, a correlation-based formula for temperature estimations in similar channels is provided and verified by both COMSOL based simulation results and experimental data of Gokaslan et al. (2022).

Without the proposed correlation-based equation of temperature estimation, it is required to use the experimental results for the same conditions as boundary conditions in order to obtain energy equation coefficients. As a solution for this constraint and in order to have the ability of making estimations regarding temperature values along the channel and in the output, by using the basic inlet values, the temperature equation is obtained and verified by the experimental results.

1.2 Literature Review

Porous medium are all around us in a daily basis, a flowing natural water spring, underground oil beds and even in our own body, our lungs, are just a few of infinite possible examples. As porous medium are mentioned, an interconnected solid matrix containing pores must be considered. The pressure drop within the medium depends on various parameters such as its porosity, permeability, fluid properties and flow velocity. First hydrodynamical analysis of the porous medium were presented by the French engineer, Henry Darcy, in the mid-1800s. In the following years of research, it has been observed that the heat transfer ratio within the porous medium is enhanced due to large contact surface of the fluid.

1.2.1 Porous medium and its classifications

1.2.1.1 Porous medium

A porous medium is a solid matrix that is partially filled by interconnected voids (pores) which can convey fluids under an applied pressure gradient. The complex structure shaping a porous medium, arise by varying pore (grain) sizes and geometries they consist of (C. T. Hsu, P. Cheng, 1990). In order to calculate any property of the porous medium, detailed information on type of the shape, dimensions, distribution and independent conductivity of consisting particles beside their interactions within the system is required (Crane & Vachon, 1977). Examples of some porous medium are shown in Figures 1.1a-1.1d (H.J. Xu, 2015).

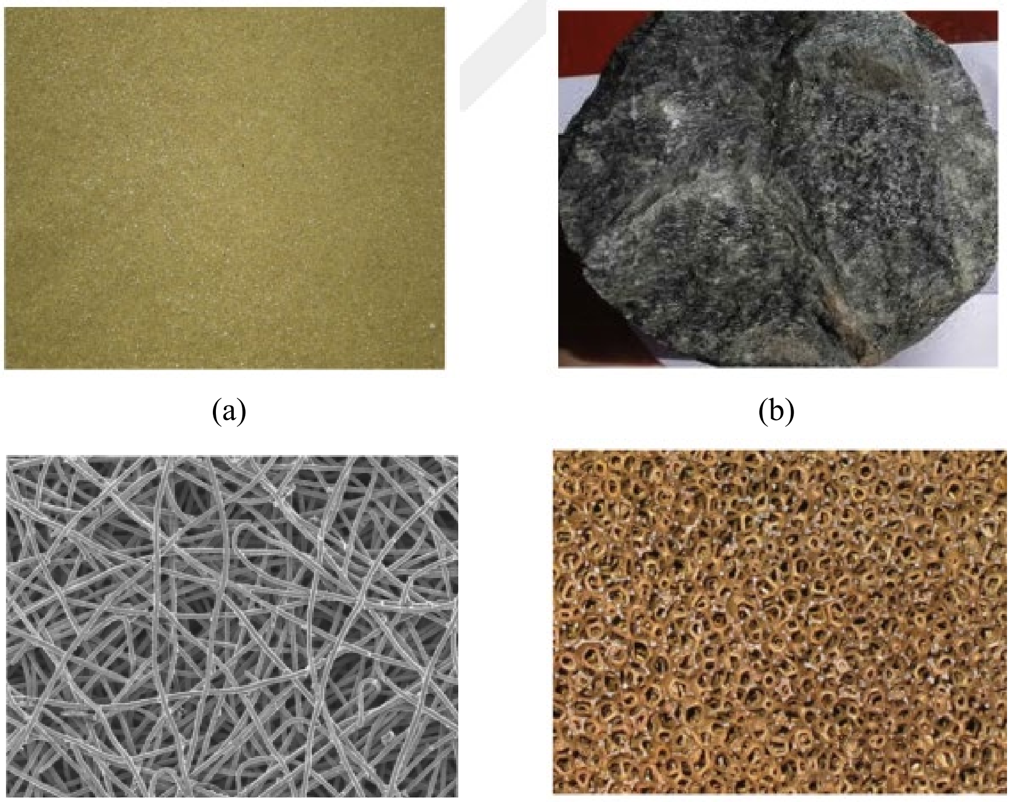

(a) (b)

(c) (d)

Figure 1.1: (a) Porous sand (b) Rocks with oil (c) Metal fiber (d) Metal foam (H.J. Xu, 2015).

The porosity of a porous medium, ε, is the ratio of void's volume (V_f), to the total volume of the medium (V) as presented in equation (1.1), or by other words, $1-\varepsilon$ is the volume occupied by the solid (V_s) to the total volume. The relation between volumes is presented in equation (1.2). While making this definition, a uniform and connected void space is considered. The value of porosity varies for every type of structure, in natural porous medium, ε is less than 0.6 while for packed beds it can be between 0.2595 and 0.4764 which are known as rhombohedral and cubic packings respectively (Donald A. Nield, 2017).

$$\varepsilon = \frac{V_f}{V} \tag{1.1}$$

$$V = V_f + V_s \tag{1.2}$$

1.2.1.2 Representative elementary volume (REV)

In order to accept a medium as porous, a representative elementary volume (REV) must be definable which may also be applicable to the whole medium. Sample of the REV representation is presented in Figure 1.2. Additionally, porosity calculated within the REV is accepted for the whole medium. Considering representative elementary volume length (ℓ) defined as $\ell = L/100$, REV dimensions required for single continuum treatment compared to other existing dimensions within the medium in Table 1.1 (Kaviany, 2005).

Permeability (K) used in definition of Brinkman screening distance, is calculated by the relation presented in the equation (1.3) in which ε represents porosity, and d_p is the particle diameter.

$$\mathrm{K} = \frac{{d_p}^2 \varepsilon^3}{180(1-\varepsilon)^2} \tag{1.3}$$

Table 1.1: Length scale requirement for single continuum treatment.

	Condition	Length Scale
Brinkman Screening Distance ($K^{1/2}$)	$K^{1/2} \ll d_p$	$10^{-12} \sim 10^{-3}$
Particle or Pore Size (d_p)	$d_p \ll \ell$	$10^{-10} \sim 10^{-2}$
REV Length (ℓ)	$\ell \ll L$	$10^{-8} \sim 1$
Linear Dimension of the System (L)		$10^{-6} \sim 10^{2}$

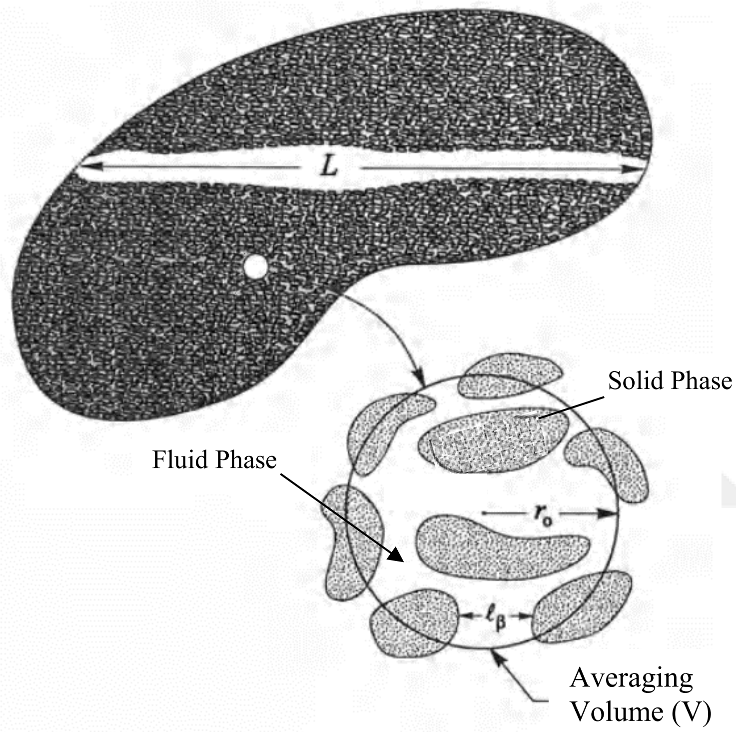

Figure 1.2: Representative Elementary Volume (REV) (Whitaker, 1973).

1.2.1.3 Classifications

The possible classifications applied may include various aspects such as, material type, natural or synthetic, homogeneity, porosity level etc. Herein, the classification is considered as material type and the corresponding thermal analysis is reviewed. While analyzing a particle based porous medium, in packed bed columns, the viscous term used in conservation of momentum equation is obtained by Ergun (1952). In other experiments investigating packed beds, a 70% deviation from Ergun equations is observed in velocity-pressure gradients, which this high level of error was related to laminar-turbulent transitions Hersman et al. (2006).

Özdemir and Özguç (1997), have studied wire screen meshes to evaluate variation of porosity and REV experimentally by making layer by layer observations. Volumes resulting in the same values at any point of the medium, except near wall regions, is considered as REV.

Air flow within compressed and un-compressed Aluminum foams with nine different pore density and porosity values have been investigated by Dukhan et al. (2006). While compressed Aluminum foams cause higher pressure drops, they have less scattered permeability values in comparison to un-compressed Aluminum foams.

1.2.1.4 Flow regimes

For a porous medium consisting of steel balls, a thorough investigation has been done upon flow regimes considering permeability-based Reynolds number (Re_K), defined in equation (1.4). The outcome has been categorized and presented in Table 1.2 (M. Özdemir, A. F. Özgüç, 1997).

$$Re_K = \frac{\rho_f U_m \sqrt{K}}{\mu_f} \tag{1.4}$$

While μ_f and ρ_f are the fluid viscousity and density respectively, and U_m is the mean velocity.

Table 1.2: Flow regime categories based on $\mathbf{Re_K}$ in porous medium of steel ball.

Flow Regime Type	Re_K Values
Darcy Flow	$Re_K < 0.062$
Forchheimer Flow	$0.340 < Re_K < 2.3$
Turbulent Flow	$Re_K > 3.4$

1.2.1.5 Channeling effect

It must be considered that in a packed bed with rigid walls, the porosity near the walls is higher, due to less efficient packing of the particles because of the walls. This non-uniform distribution of porosity within the channel, results in a velocity increase near the walls and reaches its highest value before decreasing to zero due to no-slip boundary condition. Consequently, rise of net volume flux, also known as *Channeling* *effect,* is observed. A schematic of this specific issue is presented in Figure 1.3 in which u_f, is the fluid velocity, and u_m is considered as the seepage velocity in porous medium (Donald A. Nield, 2017).

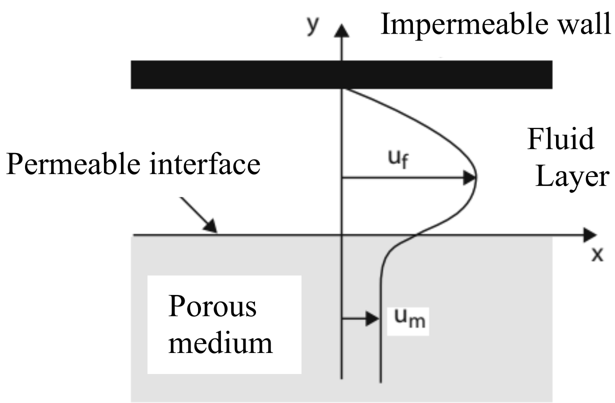

Figure 1.3: Channeling effect near walls (Donald A. Nield, 2017).

1.2.2 Flow between parallel plates

Porous medium such as packed beds, contain complex structures which makes accurate evaluations regarding their properties extremely difficult. Therefore, in order to simplify the calculations and be able to have predictions about their properties, assumptions are made which are used as their representations in form of idealized geometries as parallel plates. Utilizing such idealized geometries, has an advantage of reaching an analytical solution at pore level by which, more complex structures can be analyzed.

Vafai and Kim (1989), used the geometry in Figure 1.4 to analyze the fully developed forced convection within a granular porous medium by applying the general flow model. They were able to achieve exact solutions for temperature and velocity fields resulting in obtaining Nusselt number according to the Darcy Number.

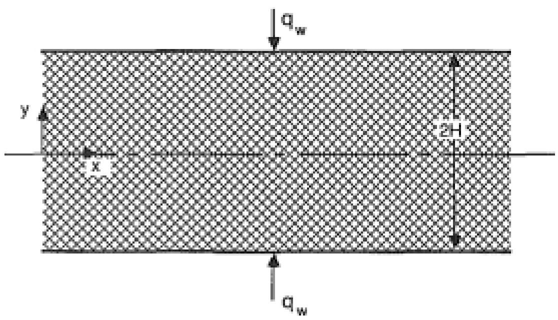

Figure 1.4: Flow along parallel plates through porous medium with constant heat flux BC (K. Vafai, S. J. Kim, 1989).

Johnson and Jacobs (1975) have studied heat transfer of immiscible fluids between parallel plates in a laminar stable flow. They have obtained the dimensionless mean temperature profile for different cases as slug flow and constant velocity. It has been observed that this mean value, is a function of axial distance.

By applying the Asymptotic method, Awad (2010) has presented a method of calculating heat transfer for thermally developing laminar flow between parallel plates for any value of the dimensionless axial coordinate. The obtained solution consists of two general cases, uniform wall temperature and uniform heat flux.

1.2.3 Flow in curved and spiral channels

Curved channel flows and spiral channels, after many studies and observations, due to the known effects of the curvilinear streamlines present in nature and applied in industrial applications, still excites researchers and is one of the fluid dynamics wonders. In natural riverbeds for instance, their stability assessment depends on accurate velocity and shear stress components analysis, even using the simplest geometries as presented in Figure 1.5. (Sk Zeeshan Ali, 2019)

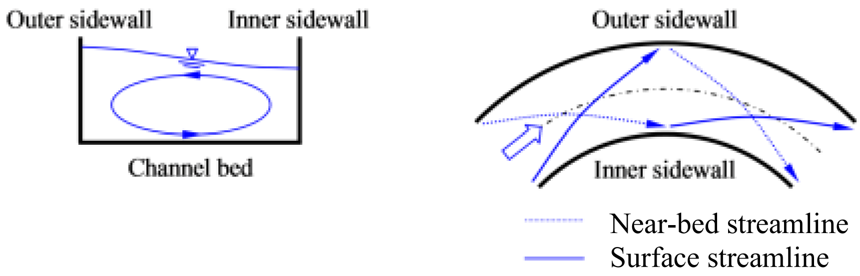

Figure 1.5: Near bed and surface streamlines in a weakly curved channel using cross-sectional and plain views (Sk Zeeshan Ali, 2019).

Hydrodynamically, except from the geometry and governing equations complexity, effects of centrifugal forces and occurrence of secondary currents, results in a three-dimensional flow which will reach an equilibrium within the system and can be considered fully developed from that point. To overcome the effects imposed by the centrifugal forces, a pressure gradient in radial direction is created which increase the applied forces to the inner wall (Sk Zeeshan Ali, 2019). Details of which are visible in Figure 1.6 in which $h(r)$ is the local flows depth at radial distance, and (r, θ, z) represent the cylindrical polar coordinates with their respective velocity components as u_r, u_θ and u_z.

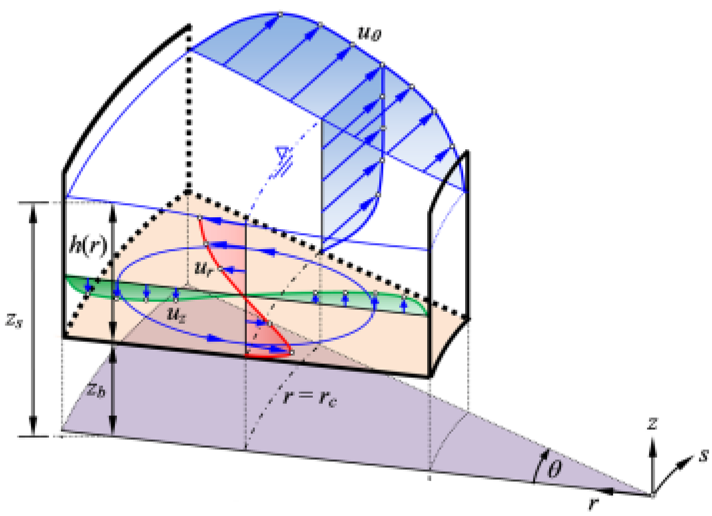

Figure 1.6: Schematic illustration of three-dimensional velocity components in a weakly curved channel using cylindrical coordinates (Sk Zeeshan Ali, 2019).

As it has been one of the important topics of countless studies in the past decades, convective heat transfer enhancement can be done by numerous methods, such as changing the flow geometry. While this methods of changing the geometry, may give the demanded enhancement under certain circumstances, it also comes with complexity, need for different/external force calculations, increase in cost etc. The formerly mentioned secondary flows, is one of the major reasons in utilizing curved channels for heat transfer enhancement, since it is known to improve both heat and mass transfer rates within curved channels. In their study, Sasmito et al. (2011), have observed the increase of heat transfer ratio in different types of spiral channels by three times higher than the straight tube.

Sasmito et al. (2011) investigated the channel types (a) straight Tube, (b) conical spiral tube, (c) in-plane spiral tube and (d) helical spiral tube as presented in Figure 1.7. Among the above, in-plane spiral tube provides the best values, followed by conical and helical spirals respectively.

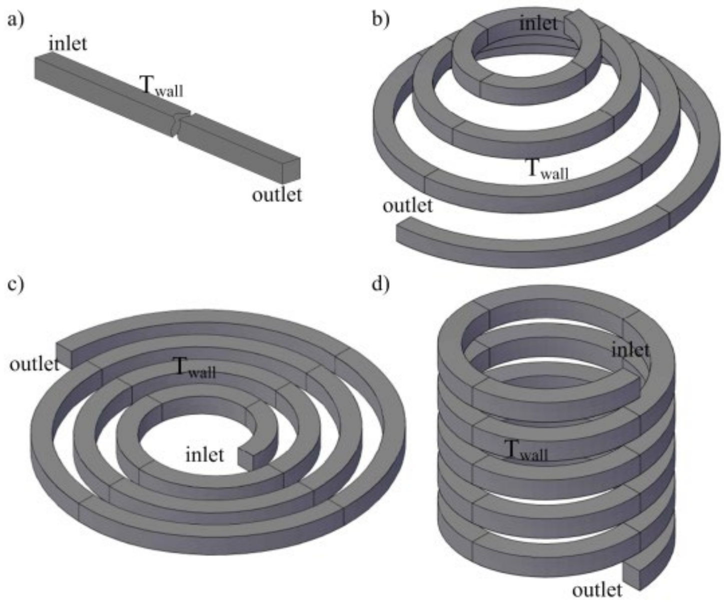

Figure 1.7: Computational domains under investigation (a) straight tube, (b) conical spiral tube, (c) in-plane spiral tube, (d) helical spiral tube (Sasmito et al, 2011).

1.2.4 Volume averaging method

The fluid flow through the voids(pores) of the porous medium, is three-dimensional and complex, and this complexity associated with the geometric shape of the medium, makes thermal and hydrodynamical analysis of such flows very difficult and expensive, preventing us from developing detailed analysis on velocity and temperature fields within the pore structures. This situation even gets more complicated as equations of a multiphase system are considered. As a result, some specific approaches are made for heat and fluid flow within porous medium. The main and widely used is the macroscopic approach within REV, which depends on defining volume averaged values of parameters utilized in the analysis such as velocity, temperature etc., besides applying the method to the governing momentum and energy equations. By applying this approach, equations which were obtained for a specific phase, can be transformed to be valid everywhere. Furthermore, the boundary conditions can also be defined and analyzed within the porous medium and create the possibility of solving such equations (Whitaker, 1973).

A sample of the representative elementary volume in volume averaging method is presented in Figure 1.8 (Kaviany, 2005).

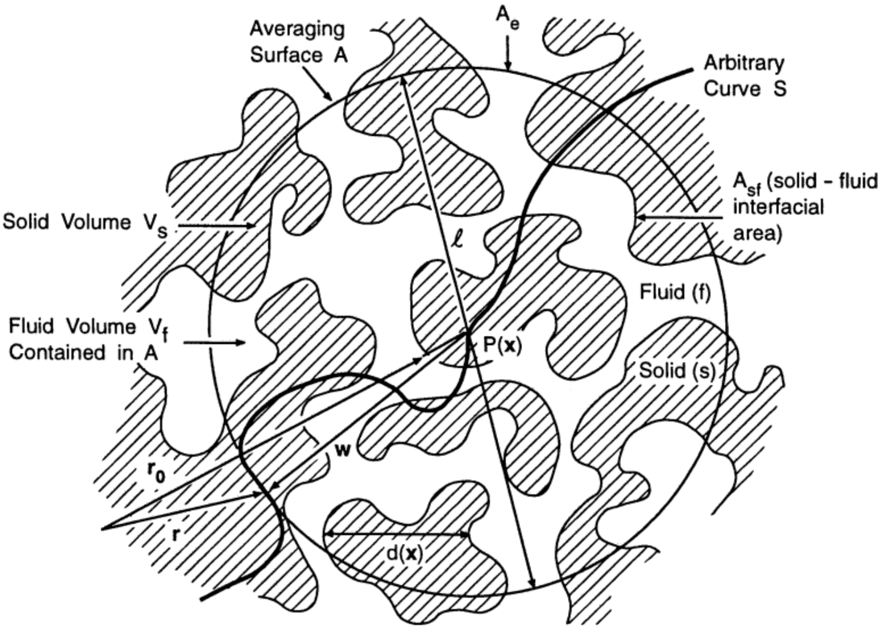

Figure 1.8: A schematic of a REV and the position vectors used with continuous fluid phase (Kaviany, 2005)**.**

In order to execute this method, averaging theorems are required for subsequent derivations. As formerly mentioned, flow through porous medium consist of fluid and solid phases, with V_f and V_s representing their occupying volumes respectively. Hence, total Volume within the porous medium (V) is defined by the relation $V_f + V_s = V$ as mentioned in equation (1.2). While considering such a multiphase flow, three different volume averaging quantities are considered. One of three, Intrinsic phase average, defines the quantity related with the k-phase, ψ_k, as in equation (1.5) which V_k is the volume of the k-phase that $k \in \{f, s\}$ with f representing fluid phase, and s the solid.

$$< \psi_k >^k = \frac{1}{V_k} \int_{V_k} \psi_k dV \tag{1.5}$$

Second type of quantity, *phase average,* is defined as equation (1.6) and is the most commonly used quantity.

$$< \psi_k > = \frac{1}{V} \int_{V_k} \psi_k dV \tag{1.6}$$

Which results to the relation presented in equation (1.7) in which $\varepsilon_k = V_k/V$ is the local volume fraction of *k*-phase

$$< \psi_k > = \varepsilon_k \ < \psi_k >^k \tag{1.7}$$

The third type, *spatial average,* is presented in equation (1.8) and assumes definition of any property ψ in both phases

$$< \psi > = \frac{1}{V} \int_V \psi \, dV \tag{1.8}$$

The volume averaged gradient of the any scalar ψ, normal to the surface **n**:

$$< \nabla \psi > = \nabla < \psi > + \frac{1}{V} \int_{A_f} \psi \boldsymbol{n} \, dA \tag{1.9}$$

For any vector $\boldsymbol{\psi}$**,** the divergence normal to surface **n** is volume averaged as

$$< \nabla . \boldsymbol{\psi} > = \nabla . < \boldsymbol{\psi} > + \frac{1}{V} \int_{A_f} \boldsymbol{\psi} . \boldsymbol{n} \, dA \tag{1.10}$$

For any vector $\boldsymbol{\psi}$**,** the curl normal to surface **n** is volume averaged as

$$< \nabla \times \boldsymbol{\psi} > = \nabla \times < \boldsymbol{\psi} > + \frac{1}{V} \int_{A_f} \boldsymbol{\psi} \times \boldsymbol{n} \, dA \tag{1.11}$$

2. MATHEMATICAL MODEL AND ANALYTICAL SOLUTIONS

2.1 Conservation Equations in General Form

Flow equations in porous materials are based on general conservation equations of mass, momentum, and energy that are considered the basics of Fluid Dynamics and Heat Transfer in all related Engineering fields. These equations are derivations of Euler equations and demonstrate the relations between velocity, pressure, density and temperature of a fluid in motion.

For a system consisting of a single-phase flow in cylindrical coordinates, it can be described as followed:

2.1.1 Conservation of mass:

Considering a straight channel as our system, mass conservation can be formulated across a specific control element of $\Delta d,$ with a fluid flowing at a velocity of u and density of ρ :

$$\begin{Bmatrix} Mass\ into\ the \\ element\ at\ d \end{Bmatrix} - \begin{Bmatrix} Mass\ out\ of\ the \\ element\ at\ d+\Delta d \end{Bmatrix} = \begin{Bmatrix} Rate\ of\ change\ of\ mass \\ within\ the\ element \end{Bmatrix}$$

Which by making mathematical operations, in its most general form it is represented as:

$$\frac{\partial \rho}{\partial t} + \nabla .(\rho \boldsymbol{V}) = 0 \tag{2.1}$$

While $\boldsymbol{V}$ is the velocity vector.

$$\boldsymbol{V} = u\overrightarrow{\iota_r} + v\overrightarrow{\iota_\varphi} + w\overrightarrow{\iota_z} \tag{2.2}$$

Substituting the velocity vector yields:

$$\frac{\partial \rho}{\partial t} + \frac{1}{r}\frac{\partial}{\partial r}(r\rho u) + \frac{1}{r}\frac{\partial}{\partial \varphi}(\rho v) + \frac{\partial}{\partial z}(\rho w) = 0 \tag{2.3}$$

2.1.2 Conservation of momentum:

Governed by Navier-Stokes equations, conservation of momentum can be defined in the following form:

$$\rho\left[\frac{\partial \boldsymbol{V}}{\partial t} + (\boldsymbol{V}.\boldsymbol{\nabla})\boldsymbol{V}\right] = -\boldsymbol{\nabla}\boldsymbol{P} + \boldsymbol{F} - \boldsymbol{\nabla} \times [\mu(\boldsymbol{\nabla} \times \boldsymbol{V})] \tag{2.4}$$

In which the left side of the equation contain the convective terms, and the right-hand side are called the diffusion terms. The former includes the acceleration and effects of non-inertial coordinates, while the latter contains hydrostatic effects, divergence of stress and body forces.

2.1.2.1 In r-direction:

$$\begin{aligned} \rho\left[\frac{Du}{Dt} - \frac{v^2}{r}\right] = {} & -\frac{\partial P}{\partial r} + F_r + 2\frac{\partial}{\partial r}\left(\mu\frac{\partial u}{\partial r}\right) \\ & + \frac{1}{r}\frac{\partial}{\partial \varphi}\left[\mu\left(\frac{1}{r}\frac{\partial u}{\partial \varphi} + \frac{\partial v}{\partial r} - \frac{v}{r}\right)\right] + \frac{\partial}{\partial z}\left[\mu\left(\frac{\partial u}{\partial z} + \frac{\partial w}{\partial r}\right)\right] \\ & + \frac{2\mu}{r}\left(\frac{\partial u}{\partial r} - \frac{1}{r}\frac{\partial v}{\partial \varphi} - \frac{u}{r}\right) \end{aligned} \tag{2.5}$$

2.1.2.2 In φ-direction:

$$\begin{aligned} \rho\left[\frac{Dv}{Dt} + \frac{uv}{r}\right] = {} & -\frac{1}{r}\frac{\partial P}{\partial \varphi} + F_\varphi + 2\frac{\partial}{\partial \varphi}\left(\frac{\mu}{r}\frac{\partial v}{\partial \varphi}\right) \\ & + \frac{\partial}{\partial r}\left[\mu\left(\frac{1}{r}\frac{\partial u}{\partial \varphi} + \frac{\partial v}{\partial r} - \frac{v}{r}\right)\right] + \frac{\partial}{\partial z}\left[\mu\left(\frac{1}{r}\frac{\partial w}{\partial \varphi} + \frac{\partial v}{\partial z}\right)\right] \\ & + \frac{2\mu}{r}\left(\frac{\partial v}{\partial r} + \frac{1}{r}\frac{\partial u}{\partial \varphi} - \frac{v}{r}\right) \end{aligned} \tag{2.6}$$

2.1.2.3 In z-direction:

$$\rho \frac{Dw}{Dt} = -\frac{\partial P}{\partial z} + F_z + 2\frac{\partial}{\partial z}\left(\mu \frac{\partial w}{\partial z}\right) + \frac{1}{r}\frac{\partial}{\partial \varphi}\left[\mu\left(\frac{1}{r}\frac{\partial w}{\partial \varphi} + \frac{\partial v}{\partial z}\right)\right] + \frac{1}{r}\frac{\partial}{\partial r}\left[\mu\left(\frac{\partial u}{\partial z} + \frac{\partial w}{\partial r}\right)\right] \tag{2.7}$$

2.1.3 Energy equation:

The total energy equation can be described as below:

$$\frac{\partial Q}{\partial t} + \Phi + k\nabla^2 T - \nabla . q_r = \rho \frac{De}{Dt} \tag{2.8}$$

$$\frac{\partial Q}{\partial t} + \Phi - \nabla . q_r + k\left(\frac{1}{r}\frac{\partial T}{\partial r} + \frac{\partial^2 T}{\partial r^2} + \frac{1}{r^2}\frac{\partial^2 T}{\partial \varphi^2} + \frac{\partial^2 T}{\partial z^2}\right) = \rho \frac{De}{Dt} \tag{2.9}$$

Including time dependent changes of Energy, convective, diffusion and dissipation terms.

2.2 Problem Formulation:

A theorical investigation of the flows within spiral channels, in which the curvature and radii follow a specific relation and pattern, are very difficult to follow and analyze. This research, profounds on experimental setup presented in Figure 2.1 and data acquired from setup by Gokaslan et al (2022), which contains an Arithmetic spiral with its radii following the relation of equation (2.10):

$$R(\varphi) = R_{min} + \frac{c\varphi}{2\pi} \quad 0 \le \varphi \le 2\pi \tag{2.10}$$

In which R_{min} is the minimum radius of spiral, and c is the channel pitch that equals to sum of fluid channel and heater channel widths, plus plate thicknesses. No matter how basic this relation maybe, the complexity of introducing both r and φ into all the conservation equations, requires valid and specific boundary conditions in order to reach an acceptable solution for the related governing equations. Therefore, assumptions are made and both geometry and flow have been simplified.

2.2.1 Assumptions:

a) Steady state

b) Fully developed laminar flow (both thermally and hydrodynamically developed)

c) No changes in Z-direction

d) Incompressible 1-D flow in φ-direction

e) Geometry simplified as cylindrical

f) No wall effects

g) Darcy flow

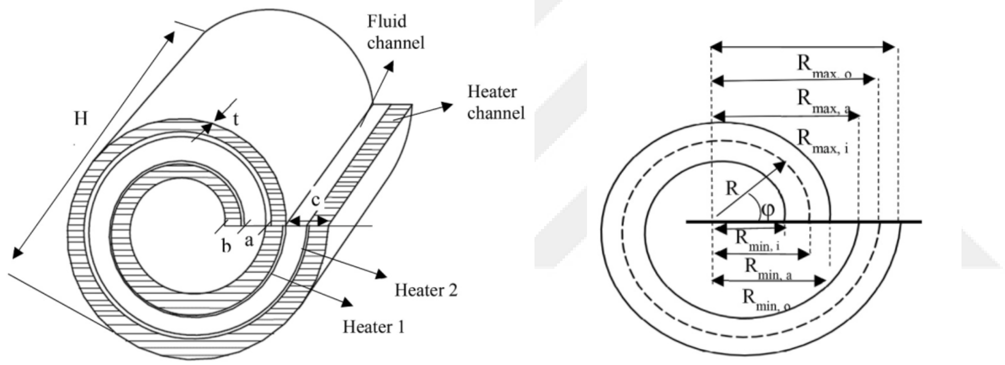

(a) (b)

Figure 2.1: Geometry of the (a) test chamber, (b) fluid channel (Gokaslan et al. 2022).

2.3 Governing Equations in Porous Medium:

2.3.1 Conservation of mass

Considering the continuity equations for incompressible flow in cylindrical coordinates and applying the volume averaging method:

$$\frac{\partial \rho_f}{\partial t} + \nabla.\langle \rho_f \boldsymbol{V} \rangle = 0 \tag{2.11}$$

By using assumptions (a) and (d) ($\langle u \rangle = \langle w \rangle = 0$) and simplifying the result, we have:

$$\frac{\partial\langle v\rangle}{\partial\varphi}=0 \tag{2.12}$$

This indicates that velocity in φ-direction, $\langle v\rangle$, is not a function of φ and do not vary with changes of φ.

2.3.2 Conservation of momentum

By applying the volume averaging method to the momentum equation, it results as:

$$\frac{\partial <\boldsymbol{V}>}{\partial t}+\rho_f <\boldsymbol{V}>.\nabla\frac{1}{\varepsilon}<\boldsymbol{V}>=-\nabla<\boldsymbol{P}>+\mu_f\nabla^2<\boldsymbol{V}>+\rho_f <\boldsymbol{f}>-\frac{\mu_f\varepsilon}{K}<\boldsymbol{V}>-\frac{F\rho_f\varepsilon}{\sqrt{K}}|<\boldsymbol{V}>|<\boldsymbol{V}> \tag{2.13}$$

In which left-hand side contains macroscopic inertial force, and right-hand side consists of pressure gradient, Brinkman viscous term (macroscopic viscous shear stress), body forces, Darcy term (microscopic viscous shear stress) and Ergun inertial term (microscopic inertial force) respectively. Besides, F is the Forchheimer coefficient and K is the permeability, calculated as presented in equation (1.3).

Now the momentum equation must separately be considered in all directions of the investigated geometry:

2.3.2.1 *r*-direction

$$\begin{aligned}\frac{\partial\langle u\rangle}{\partial t}+\frac{\rho_f}{\varepsilon}\left[\langle u\rangle\frac{\partial\langle u\rangle}{\partial r}+\frac{\langle v\rangle}{r}\frac{\partial\langle u\rangle}{\partial\varphi}+\langle w\rangle\frac{\partial\langle u\rangle}{\partial z}-\frac{\langle v\rangle^2}{r}\right]&=-\frac{\partial\langle P\rangle}{\partial r}\\&+\mu_f\left[\frac{1}{r}\frac{\partial}{\partial r}\left(r\frac{\partial\langle u\rangle}{\partial r}\right)+\frac{1}{r^2}\frac{\partial^2\langle u\rangle}{\partial\varphi^2}+\frac{\partial^2\langle u\rangle}{\partial z^2}-\frac{\langle u\rangle}{r^2}\right.\\&\left.-\frac{2}{r^2}\frac{\partial\langle v\rangle}{\partial\varphi}\right]+\langle\rho_f f_r\rangle-\left(\frac{\mu_f\varepsilon}{K}\right)\langle u\rangle-\left(\frac{F\rho_f\varepsilon}{\sqrt{K}}\right)|\boldsymbol{V}|\langle u\rangle\end{aligned} \tag{2.14}$$

Considering the assumptions (a), (d), (f) and (g), it simplifies to

$$\frac{\rho_f}{\varepsilon}\frac{\langle v\rangle^2}{r}=\frac{\partial\langle P\rangle}{\partial r} \tag{2.15}$$

2.3.2.2 φ-direction

$$\frac{\partial\langle v\rangle}{\partial t}+\frac{\rho_f}{\varepsilon}\left[\langle u\rangle\frac{\partial\langle v\rangle}{\partial r}+\frac{\langle v\rangle}{r}\frac{\partial\langle v\rangle}{\partial\varphi}+\langle w\rangle\frac{\partial\langle v\rangle}{\partial z}+\frac{\langle u\rangle\langle v\rangle}{r}\right]$$
$$=-\frac{1}{r}\frac{\partial\langle P\rangle}{\partial\varphi}$$
$$+\mu_f\left[\frac{1}{r}\frac{\partial}{\partial r}\left(r\frac{\partial\langle v\rangle}{\partial r}\right)+\frac{1}{r^2}\frac{\partial^2\langle v\rangle}{\partial\varphi^2}+\frac{\partial^2\langle v\rangle}{\partial z^2}-\frac{\langle v\rangle}{r^2}\right. \tag{2.16}$$
$$\left.+\frac{2}{r^2}\frac{\partial\langle u\rangle}{\partial\varphi}\right]+\langle\rho_f f_\varphi\rangle-\left(\frac{\mu_f\varepsilon}{K}\right)\langle v\rangle-\left(\frac{F\rho_f\varepsilon}{\sqrt{K}}\right)|\boldsymbol{V}|\langle v\rangle$$

With applying assumptions (a), (d), (f) and (g), it takes the form

$$0=-\frac{1}{r}\frac{\partial\langle P\rangle}{\partial\varphi}-\left(\frac{\mu_f\varepsilon}{K}\right)\langle v\rangle \tag{2.17}$$

Considering assumption (b), pressure drop in the φ-direction can be inerpreted as a constant, C_φ which results in

$$\frac{\partial\langle P\rangle}{\partial\varphi}= C_\varphi\Rightarrow\langle P\rangle(\varphi)=C_\varphi\,.\varphi+c_1 \tag{2.18}$$

2.3.2.3 z-direction

$$\frac{\rho_f}{\varepsilon}\left[\langle u\rangle\frac{\partial\langle w\rangle}{\partial r}+\frac{\langle v\rangle}{r}\frac{\partial\langle w\rangle}{\partial\varphi}+\langle w\rangle\frac{\partial\langle w\rangle}{\partial z}\right]$$
$$=-\frac{\partial\langle P\rangle}{\partial z}+\mu_f\left[\frac{1}{r}\frac{\partial}{\partial r}\left(r\frac{\partial\langle w\rangle}{\partial r}\right)+\frac{1}{r^2}\frac{\partial^2\langle w\rangle}{\partial\varphi^2}+\frac{\partial^2\langle w\rangle}{\partial z^2}\right] \tag{2.19}$$
$$-\left(\frac{\mu_f\varepsilon}{K}\right)\langle w\rangle-\left(\frac{F\rho_f\varepsilon}{\sqrt{K}}\right)|\boldsymbol{V}|\langle w\rangle$$

Using assumptions (a), (d), (f) and (g), it takes the form

$$0=\frac{\partial\langle P\rangle}{\partial z} \tag{2.20}$$

Which indicates no dependency of the pressure to values in z-direction.

Now by simplifying the equation (2.17) and inserting C_φ, velocity in φ-direction can be presented as

$$\langle v \rangle = -\frac{KC_\varphi}{r\mu_f\varepsilon} \tag{2.21}$$

By substituting acquired relation for $\langle v \rangle$ in equation (2.15), it takes the form:

$$\frac{\partial\langle P \rangle}{\partial r} = \frac{\rho_f}{\varepsilon r}\left(-\frac{KC_\varphi}{r\mu_f\varepsilon}\right)^2 \tag{2.22}$$

$$\langle P \rangle(r) = -\frac{\rho_f}{2\varepsilon^3 r^2}\left(\frac{KC_\varphi}{\mu_f}\right)^2 + c_2 \tag{2.23}$$

Now merging the equations of $\langle P \rangle$ and considering $c_3 = c_1 + c_2$

$$\langle P \rangle(r,\varphi,z) = -\frac{\rho_f}{2\varepsilon^3 r^2}\left(\frac{KC_\varphi}{\mu_f}\right)^2 + C_\varphi\,.\varphi + c_3 \tag{2.24}$$

By applying the following boundary condition $\langle P \rangle(r_m, 0, z) = P_1$, where $r_m = r_o + r_i/2$, the equation (2.24) becomes

$$\langle P \rangle(r,\varphi,z) = -\frac{\rho_f}{2\varepsilon^3 r^2}\left(\frac{KC_\varphi}{\mu_f}\right)^2\left(\frac{1}{r_m{}^2} - \frac{1}{r^2}\right) + C_\varphi\,.\varphi + P_1 \tag{2.25}$$

2.3.3 Mean velocity

The mean velocity through cross sectional area (A) of the channel is acquired by utilizing equation (2.26), using the velocity in φ-direction as presented in equation (2.21), channel height (H) and along channel width from inner wall (r_i) to outer wall (r_o).

$$U_m = \frac{1}{A}\int\langle v \rangle dA = \frac{1}{H(r_o - r_i)}\int_{r_i}^{r_o}\int_0^H -\frac{KC_\varphi}{r\mu_f\varepsilon}drdz \tag{2.26}$$

Which simplifies to

$$U_m = -\frac{KC_\varphi}{\varepsilon\,\mu_f(r_o - r_i)} ln\left(\frac{r_o}{r_i}\right) \tag{2.27}$$

2.3.4 Energy equation

Energy equations of fluid and solid phases in a porous medium are demonstrated in equations (2.28) and (2.29) respectively

$$\rho_f C_{P,f}\left(\frac{\partial T_f}{\partial t} + \vec{\nabla}.\boldsymbol{V}T_f\right) = k_f \nabla^2 T_f \tag{2.28}$$

$$\rho_s C_{P,s}\frac{\partial T_s}{\partial t} = k_s \nabla^2 T_s \tag{2.29}$$

Microscopic approach has been used, and thermal non-equilibrium is considered for the relations above.

Effective thermal conductivity (k_{eff}) or bulk thermal conductivity coefficient (k_{sf}) as presented in equation (2.31), is calculated using weighted average of the Maxwell upper bound according to fluid (k_f) and solid (k_s) phases, which is the most accurate in comparison to values obtained by experimental results, introducing an adjustable function $f_0 = 0.8 + 0.1\varepsilon$ and α_0 calculated as in equation (2.30) (Hadley, 1986):

$$log\,\alpha_0 = -1.084 - 6.778(\varepsilon - 0.298)\ \ for\ \ 0.298 \le \varepsilon \le 0.580 \tag{2.30}$$

$$\begin{aligned}\frac{k_{eff}}{k_f} &= (1-\alpha_0)\frac{\varepsilon f_0 + k_s/k_f\,(1-\varepsilon f_0)}{1-\varepsilon(1-f_0) + k_s/k_f\,\varepsilon(1-f_0)} \\ &\quad + (\alpha_0)\frac{2(1-\varepsilon)\left(k_s/k_f\right)^2 + (1+2\varepsilon)k_s/k_f}{(2+\varepsilon)\,k_s/k_f + 1 - \varepsilon}\end{aligned} \tag{2.31}$$

Applying the volume averaging method to acquire the macroscopic relations and considering LTE, for a continuous porous domain the energy equation yields

$$\begin{aligned}(\rho c_P)_{sf}\frac{\partial\langle T\rangle}{\partial t} &+ \rho_f c_{Pf}\langle \boldsymbol{V}\rangle.\nabla\langle T\rangle \\ &= k_{sf}\overrightarrow{\nabla^2}\langle T\rangle - \nabla.\left[\frac{1}{V}\int_V \left(k_f - k_s\right)T dS\right] - \rho_f c_{Pf}\nabla.\langle T'\boldsymbol{V}'\rangle\end{aligned} \tag{2.32}$$

In which, last two terms of the equation (2.32) are known as tortuosity and thermal dispersion. These two terms are result of applying volume averaging method, and do not exist in the microscopic form of the equations.

Now assuming thermal dispersion in form of thermal diffusion transport, we have

$$k_d \nabla^2 \langle T \rangle = -\rho_f c_{Pf} \nabla . \langle T' \boldsymbol{V}' \rangle \tag{2.33}$$

Therefore, the equation (2.32) takes the form presented in equation (2.34). It must be noted that the tortuosity term is neglected, regarding the change of thermal diffusion due to microstructure of the solid porous matrix.

$$(\rho c_P)_{sf} \frac{\partial \langle T \rangle}{\partial t} + \rho_f c_{Pf} \langle \boldsymbol{V} \rangle . \nabla \langle T \rangle = k_{tot} \nabla^2 \langle T \rangle \tag{2.34}$$

The term k_{tot} equals to summation of thermal dispersion conductivity (k_d) and effective thermal conductivity (k_{eff}).

Simplifying the equation (2.34) and considering the assumptions (a), (b) and (d), it becomes

$$\begin{aligned} \rho_o C_o \frac{\partial \langle T \rangle}{\partial t} + \rho_f C_{p,f} \left(\langle u \rangle \frac{\partial \langle T \rangle}{\partial r} + \frac{\langle v \rangle}{r} \frac{\partial \langle T \rangle}{\partial \varphi} + \langle w \rangle \frac{\partial \langle T \rangle}{\partial z} \right) \\ = k_{tot} \left[\frac{1}{r} \frac{\partial \langle T \rangle}{\partial r} + \frac{\partial^2 \langle T \rangle}{\partial r^2} + \frac{1}{r^2} \frac{\partial^2 \langle T \rangle}{\partial \varphi^2} + \frac{\partial^2 \langle T \rangle}{\partial z^2} \right] \end{aligned} \tag{2.35}$$

$$\rho_f C_{p,f} \left(\frac{\langle v \rangle}{r} \frac{\partial \langle T \rangle}{\partial \varphi} \right) = k_{tot} \left[\frac{1}{r} \frac{\partial \langle T \rangle}{\partial r} + \frac{\partial^2 \langle T \rangle}{\partial r^2} \right] \tag{2.36}$$

Due to the assumption of thermally fully developed flow, it can be considered

$$\frac{\partial^2 \langle T \rangle}{\partial \varphi^2} = 0 \tag{2.37}$$

$$\frac{\partial \langle T \rangle}{\partial \varphi} = constant = C_T \tag{2.38}$$

$$\langle T \rangle (\varphi) = C_T . \varphi + C_4 \tag{2.39}$$

Now substituting C_T and velocity relations into equation (2.36), we have

$$\rho_f C_{p,f}\left(\frac{-KC_\varphi}{r^2\mu_f}C_T\right) = k_{tot}\left[\frac{1}{r}\frac{\partial\langle T\rangle}{\partial r}+\frac{\partial^2\langle T\rangle}{\partial r^2}\right] \tag{2.40}$$

By introducing the coefficient J and simplifying, the equation (2.40) is solved as in equation (2.41)

$$\langle T\rangle(r) = \frac{J}{2}.ln^2(r) + c_5.ln(r) + c_6 \tag{2.41}$$

$$J = \frac{-\rho_f C_{p,f} K C_\varphi C_T}{k_{tot}\,\mu_f} \tag{2.42}$$

Now combining equations (2.39) and (2.41) to reach a general equation for $\langle T\rangle(r,\varphi)$, and assuming $C_7 = C_4 + C_6$, we get

$$\langle T\rangle(r,\varphi) = \frac{J}{2}.ln^2(r) + c_5.ln(r) + C_T.\varphi + C_7 \tag{2.43}$$

which can be solved using the boundary conditions (2.44) and (2.45),

$$\langle T\rangle(r_m, 0) = T_{in} \tag{2.44}$$

$$\left.\frac{\partial\langle T\rangle}{\partial r}\right|_{r_m} = \frac{-q"_w}{k_{eff}} \tag{2.45}$$

With

$$C_5 = \frac{-q"r_m}{k_{tot}} - J.ln\,(r_m) \tag{2.46}$$

$$C_7 = T_{in} - \frac{J}{2}.ln^2(r_m) + \left(\frac{q"r_m}{k_{tot}} + J.ln\,(r_m)\right)ln(r_m) \tag{2.47}$$

That with substituting into equation (2.43) and simplifying it, result in equation (2.47) as the final form of the energy equation for so considered assumptions

$$\langle T\rangle(r,\varphi) = \frac{J}{2}.ln^2\left(\frac{r_m}{r}\right) + \frac{q"r_m}{k_{tot}}.ln\left(\frac{r_m}{r}\right) + C_T.\varphi + T_{in} \tag{2.48}$$

It is observed and also presented in Chapter 4, that the values obtained by equations (2.48) are in complete agreement with the experimental values up to 270 degrees and confirm solution legitimacy. It must be considered that the values after 270 degrees of the experiment, as discussed by Gokaslan et al (2022), due to heat loss caused by the fin effect in solid structure of the channel surface and header surface, are lower than the values measured within the channel up to that region, and therefore are not considered in evaluation and comparison processes.

2.3.5 Correlation based C_T

As previously mentioned in equation (2.48), the critical value of C_T, which is the major coefficient affecting the overall temperature output of the formula presented in equation (2.49), is based on experimental results obtained on the domain. This vital constraint prohibits acquiring any result analytically or having a proper estimation regarding the overall possible output of the system without formerly finalizing the experiments and calculating the corresponding $C_T$values. As a contribution to literature, for spiral heat exchangers filled with AISI 1010 steel balls following the formerly discussed assumptions, a correlation as presented in the equation (2.49) is obtained considering imposed heat flux on the walls (q"), fluid thermal conductivity (k_f) and viscosity (μ_f), initial flow debi ($\dot{m}$.), particle diameter (d_p) and channel width (d) as the critical factors affecting the output temperature and verified by the existing experimental data.

$$C_T = \frac{a\, q"\, \mu_f}{\dot{m}\, k_f\, \pi}\left(\frac{d_p}{d}\right)^b \tag{2.49}$$

In which coefficients a and b are calculated for different flow states based on Re_{dh}values and accordingly, equation (2.49) takes the form below

$$a = 1.6379\,, b = 0.98463 \qquad \boldsymbol{Re_{dh} \geq 1500} \tag{2.50}$$

$$a = 0.3424\,, b = 0.05313 \qquad \boldsymbol{Re_{dh} < 1500} \tag{2.51}$$

Consequently, equation (2.48) will take following form for temperature estimations regardless of the experimental results, and is a correlation only based on the input values:

$$\langle T\rangle(r,\varphi)=\frac{J}{2}.\,ln^2\left(\frac{r_m}{r}\right)+\frac{q"r_m}{k_{tot}}.\,ln\left(\frac{r_m}{r}\right)+\left(\frac{a\;q"\;\mu_f}{\dot{m}\;k_f\;\pi}\left(\frac{d_p}{d}\right)^b\right).\,\varphi+T_{in} \qquad (2.52)$$

3. COMSOL MULTIPHYSICS SIMULATION DETAILS

3.1 Software Review

COMSOL Multiphysics is a mathematical modeling software used in vast fields of engineering and scientific research, first starting as a MATLAB add-in. Its comprehensive material library and detailed parameter-based models give the opportunity to freely simulate and evaluate the demanded system according to the existing conditions and parameters with accurate results while compared to experimental data.

The space dimension options for the system designs consist of 3D, 2D Axisymmetric, 2D, 1D Axisymmetric, 1D and point based as presented in Figure 3.1.

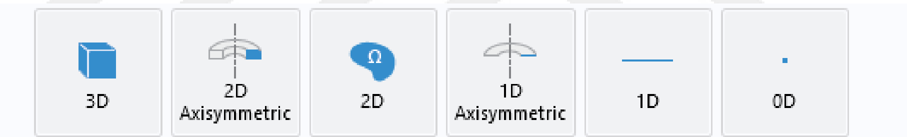

Figure 3.1: COMSOL Multiphysics Space Dimension Options.

The physics interfaces on the other hand vary from AD/DC, Radio Frequency, Semi-Conductors, Optics, and Acoustics, to Structural Mechanics, Heat Transfer, Fluid Flow, Plasma, Chemical Species Transport and Electrochemistry Analysis. Each of the mentioned physics interfaces are divided into very specific sub-interfaces. As most related to our topic, sub-interfaces of Heat Transfer and Fluid Flow are presented in Figures 3.2a and 3.2b respectively

Another valuable asset of COMSOL Multiphysics is the Mathematics Interface which is suitable for solving PDEs and ODEs based on your geometry and conditions, performing sensitivity analysis, modeling moving meshes and deformed geometries, and more.

.

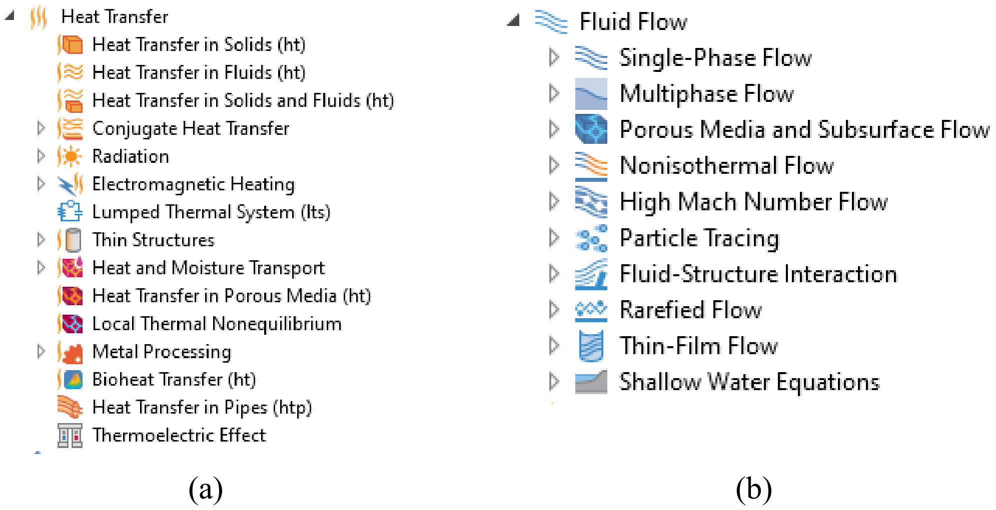

Figure 3.2: (a) Heat Transfer Sub-interface (b) Fluid Flow Sub-interface.

3.2 Model Details and Parameters

Considering the channel geometry, flow details and assumptions made in Chapter 2, the 2D geometry is selected in the space dimension section, and arithmetic spiral following equation (2.10) is created and added as the simulation domain. The geometry is based on channel TC2 of the experimental setup of Gokaslan (2022), with 15 mm channel width. The applied geometry is presented in Figure 3.3.

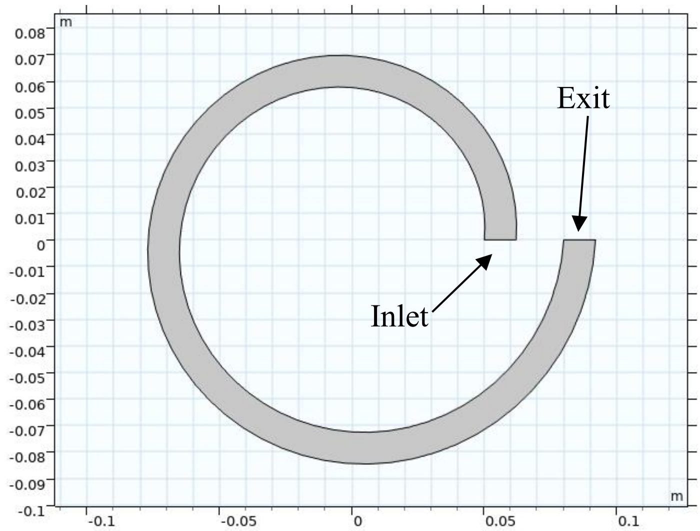

Figure 3.3: Schematic of the simulation domain geometry.

As the first step in selection of physics interface, Free and Porous Media Flow is chosen under Fluid Flow, which is an interface for computation of pressure and velocity fields of single-phase flows. This physics interface suits the flow in channels described by the Navier-Stokes equations and is suitable for both steady-state and time-dependent analysis.

For analysis of thermal aspects, Heat Transfer in Porous Media is selected under Heat Transfer interface. Despite in Fluid Flow interface, there are not too many options for porous media analysis on thermal basis and this is the only interface available but a very comprehensive one. This interface models heat transfer by conduction, convection, and radiation. Averaging models is used for defining of temperature equation in this interface that makes it accountable for both solid matrix and fluid properties and is applicable to stationery and time dependent domains.

3.3 Added Materials and Properties

As mentioned before, COMSOL Multiphysics comes with a material library which includes most of the required properties of the materials, besides let you add a missing property which relies on your simulation details or modify an existing one according to your specific conditions.

Therefore, Air has been chosen from included library as fluid material for the domain in order to simulate the experiment conditions. Unfortunately, material library lacks AISI 1010 which is the material utilized as steel balls for the porous matrix and the properties of the material has been manually added on each step to the Model Builder of software.

For both Fluid Flow and Heat Transfer Analysis, 12691 mesh elements are considered to obtain the most accurate and realistic results. A detailed view on the mesh structure is presented in Figures 3.4 and 3.5.

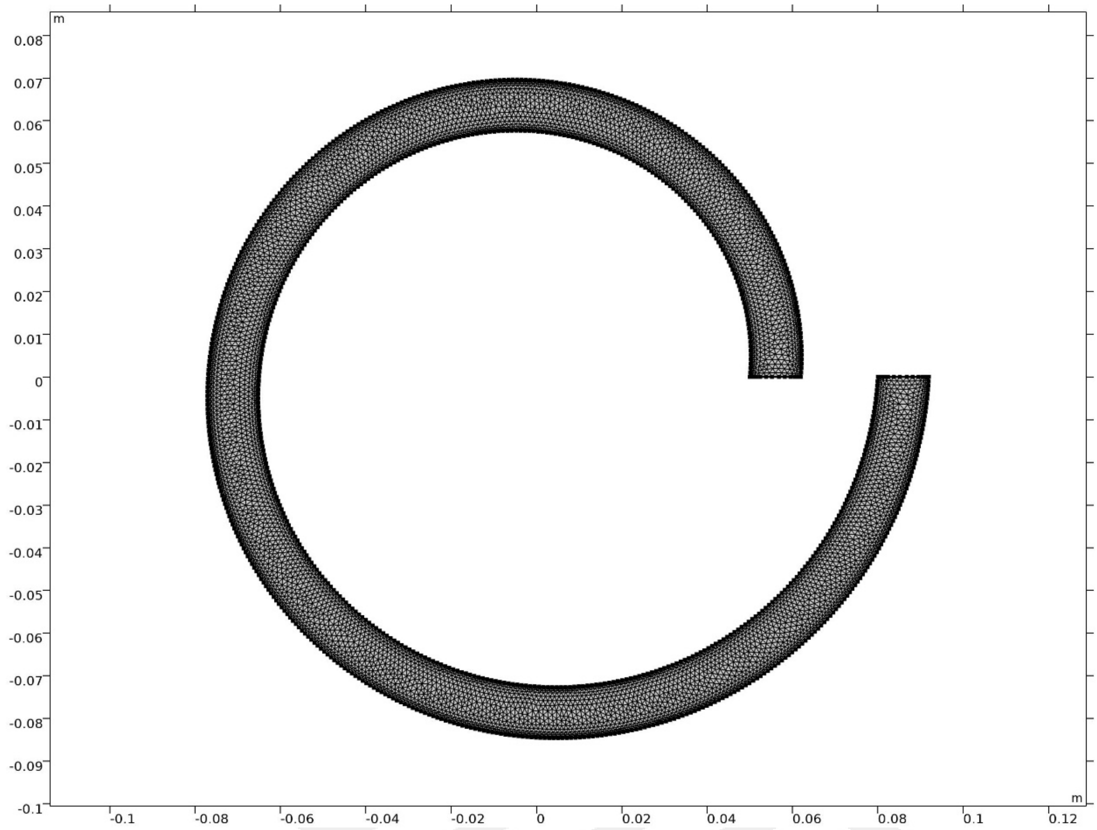

Figure 3.4: Domain geometry mesh structure view.

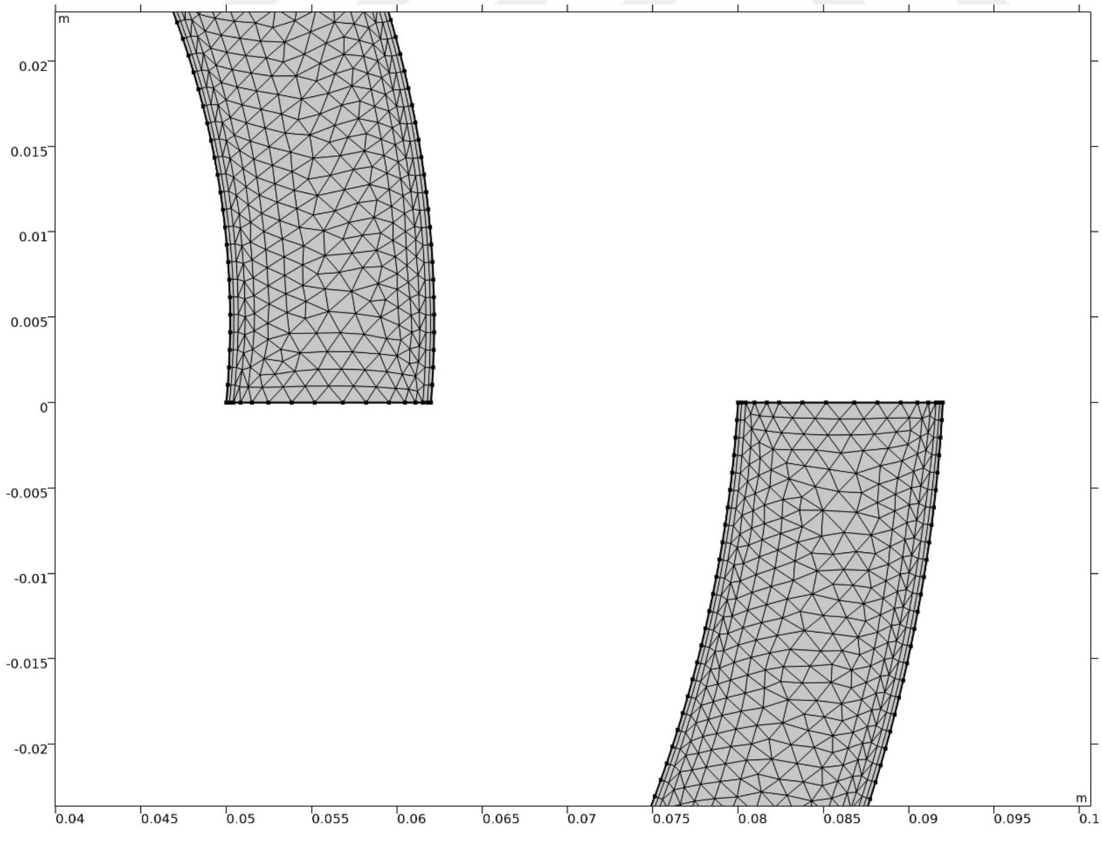

Figure 3.5: Close-up view of the mesh structure of the simulation domain in exit and entrance region.

3.4 Boundary and Initial Conditions

3.4.1 Fluid flow

Initial conditions applied under fluid flow interface are assuming a fully developed flow on the inlet region and indicating the flow rate under Fully Developed Flow section for inlet. Atmospheric pressure is also assumed on the inlet section. Walls are considered with zero movement and fixed. Except fluid properties which are known from material library, porous matrix properties of Porosity and Permeability are also added manually.

Boundary conditions on the output region is assuming a known average pressure according to the experimental data. Another possible applicable boundary condition would be assumption of a fully developed flow with a known value of outlet pressure, which do not affect the final results as compared to average pressure BC.

3.4.2 Heat transfer

As the first step, volume averaging method is selected for effective conductivity analysis under porous medium settings, heat conduction, density and heat capacity of the porous matrix besides porosity values are also added. The initial and developing pressure and velocity values are considered linked to the fluid flow calculation interface.

For the domain initial value, temperature known from the experiments is added and no thermal insulation is considered on any boundaries of the domain. Inflow temperature and pressure values are added for upstream properties. Constant wall heat flux conditioned is added, considering same heat flux values on both walls through the domain.

3.5 Results

The COMSOL Multiphysics simulation is run for TC2 channel and flow properties of Gokaslan (2022). The variations according to particle diameter of the porous matrix, imposed heat flux, inlet flow rates and pressure drop are the parameters affecting the output. For particle diameter (d_p) of 2mm, 19 different flow rates, for particle diameter of 2.38mm, 17 different flow rates and for particle diameter of 3.17mm, 16 different flow rates have been studied.

Obtained results for pressure gradient and temperature distribution are in good agreement with the experimental results. However, velocity values cannot be verified since the experimental setup lacks velocity measurements along he channels and on the outlet section.

As a sample, results for porous medium consisting of particle with 3.17mm diameter is presented in Figures 3.6, 3.7, 3.8, 3.9 which are for temperature distribution surface, isothermal contour, pressure distribution contour and velocity magnitude respectively.

These results belong to inlet flow value of 3.067 g/s, with heat fluxes of 219 W/m^2 and 214 W/m^2 applied on inner and outer walls of the channel respectively.

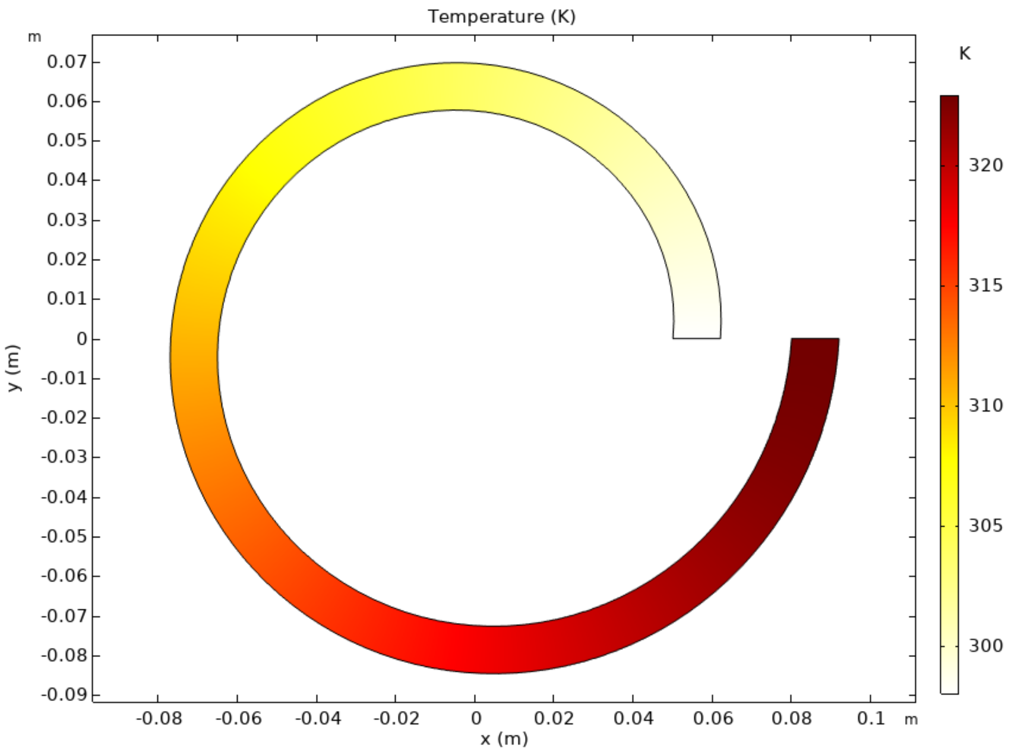

Figure 3.6: Temperature distribution within porous channel.

The details of the results obtained, and their accuracy will be discussed in Chapter 4, while compared with experimental and analytical values. Furthermore, all the graphs obtained as outputs of the simulation results are presented in Appendix A.

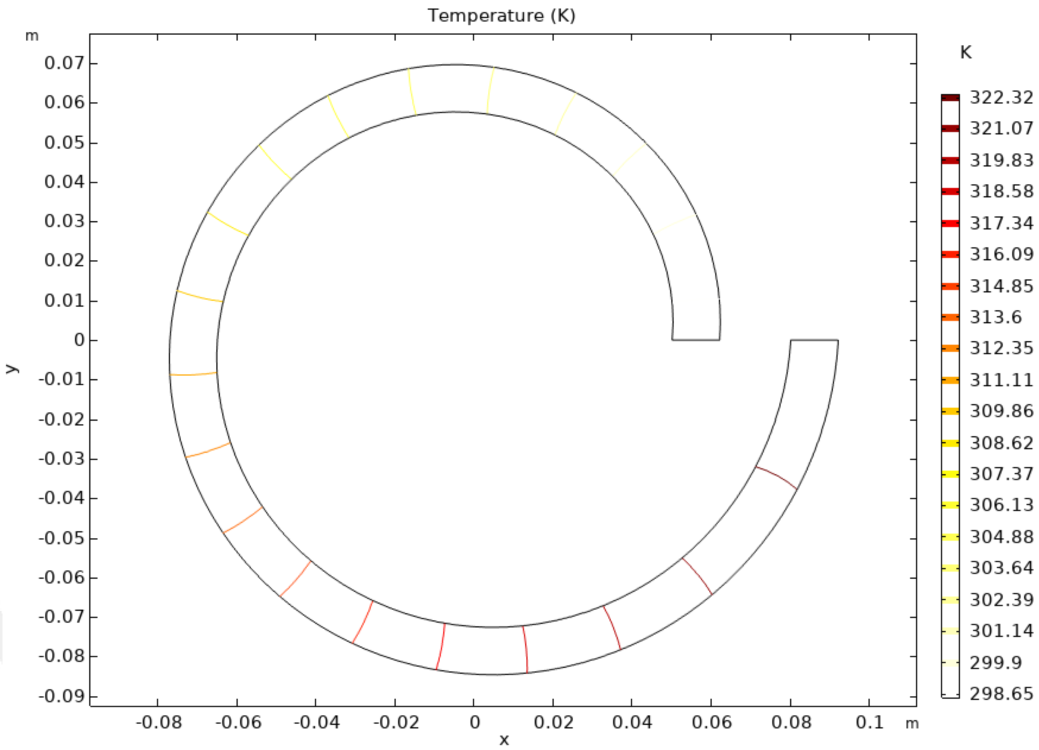

Figure 3.7: Isothermal contours within porous channel.

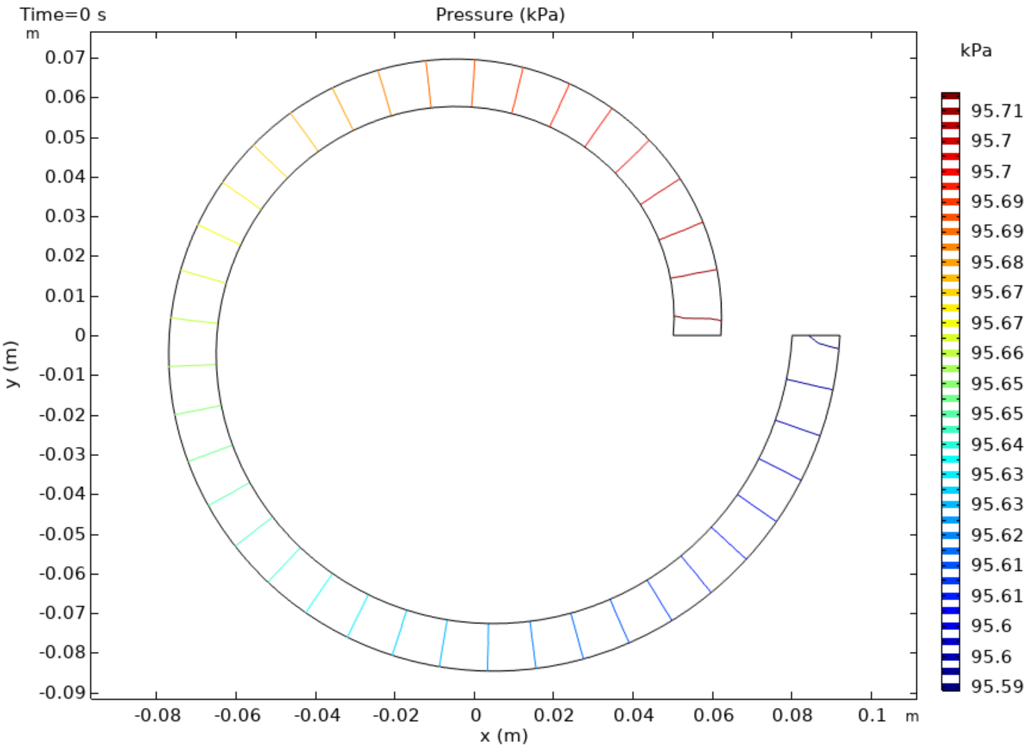

Figure 3.8: Pressure distribution within porous channel.

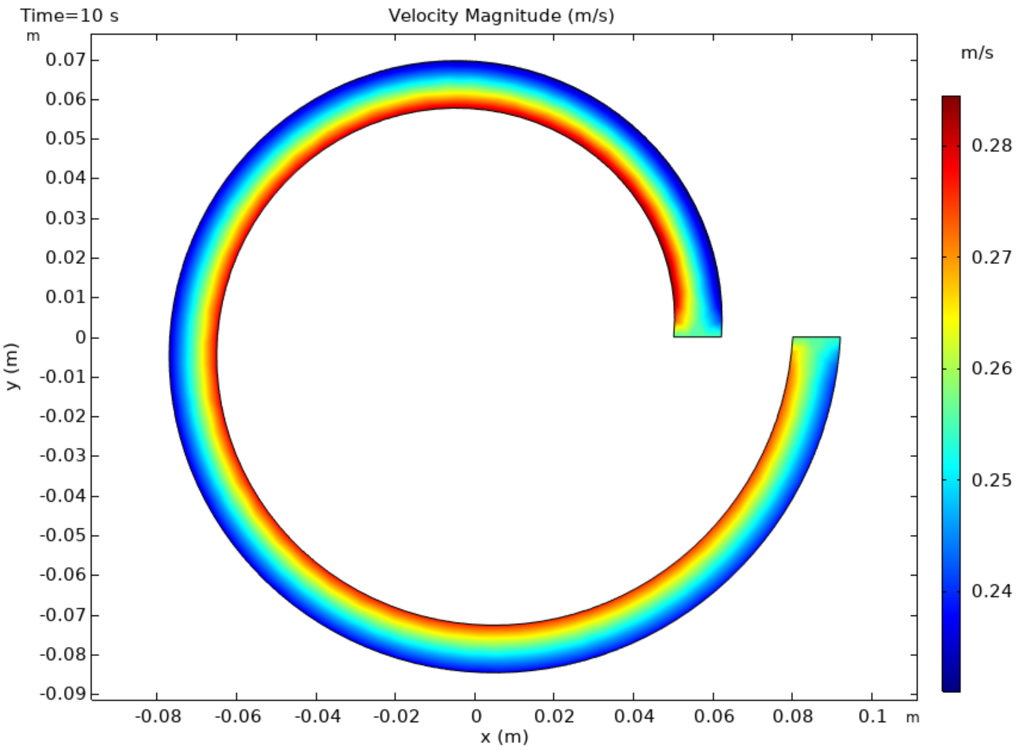

Figure 3.9: Velocity magnitude within porous channel.

3.6 Mesh Dependency

As previously discussed in section 3.3, the COMSOL simulations have been executed utilizing 12691 mesh elements, and all the results are based upon this mesh structure. The reason for applying this number of mesh elements which is also the maximum value available for this geometry, is based on the temperature results from comparison of different number of mesh elements that the details of the results for three selected number of elements (12691, 506 and 61) are presented in Table 3.1, and the results from these simulations compared to the experimental data by Gokaslan et al. (2022) are shown in Figure 3.10 for inlet flow value of 3.067 g/s, with heat fluxes of 219 W/m^2 and 214 W/m^2 applied on inner and outer walls of the channel respectively.

Evaluation of the results presented in Table 3.1 and Figure 3.10, indicates low dependency of the simulation results on the number of mesh elements especially on the entrance and exit region of the channel with %0.08 difference in calculated values utilizing 12691 mesh elements vs. 61 mesh elements on the channel exit. Whilst considering middle part of the channel, maximum difference in results for utilized mesh elements arise up to %3.79 considering values by 12691 mesh elements vs. 61 mesh elements as the maximum and minimum number of utilized mesh elements.

Table 3.1: Simulation result error of different mesh element numbers vs experimental data.

Evaluated Position (Degrees along channel)	12691 Elements	506 Elements	61 Elements	Error ratio within results of max. & min. mesh element numbers
90	8.96%	9.81%	10.39%	1.57%
180	5.99%	7.46%	9.45%	3.68%
270	5.26%	7.11%	8.85%	3.79%
360	0.98%	1.00%	0.90%	0.08%

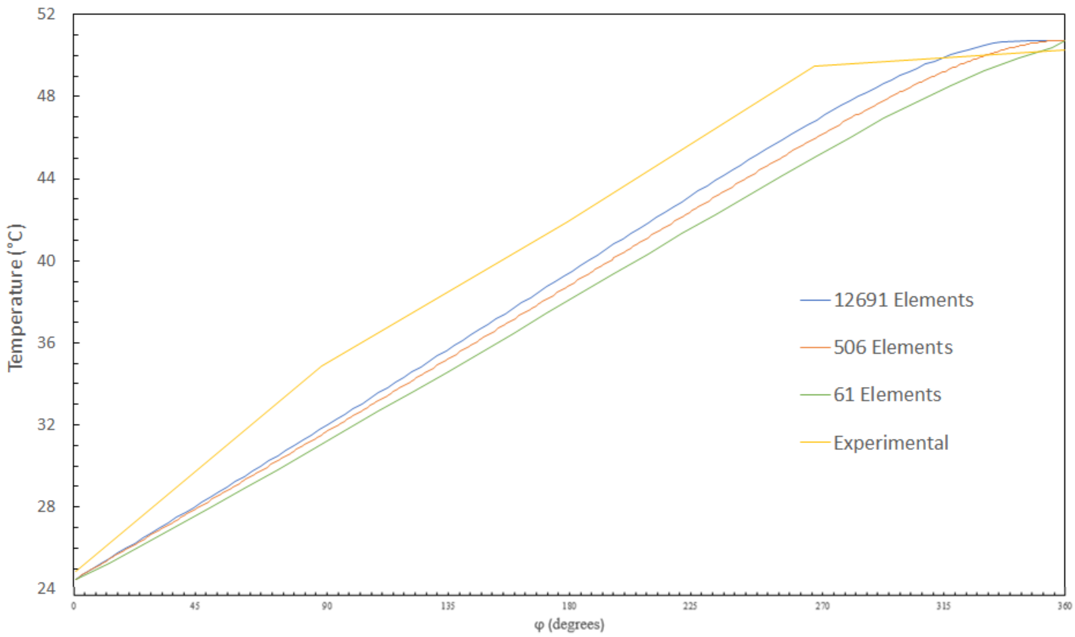

Figure 3.10: Simulation result of different mesh element numbers vs experimental data.

Despite low difference in the results of all number of mesh elements, in order to minimize the error vs experimental data by Gokaslan et al. (2022), 12691 mesh elements is utilized for COMSOL simulations, since it has minimum error vs experimental values in the middle part of the channel compared to results obtained by utilizing 506 and 61 number of mesh elements.

4. RESULTS AND DISCUSSION

Results obtained by all the formerly mentioned methods, analytical solution, COMSOL simulations, correlation-based solution and experimental data are all presented and used for evaluation of their accuracy and similarity to experimental data obtained by Gokaslan et al. (2022).

4.1 Analytical Solution Results

Results of the temperature values within the channel based on the equation (2.48) for porous medium consisting of particles with 3.17mm diameter are presented. In order to analyze the results obtained by analytical solution, the equation is solved for thermal dispersion conductivity (k_d) in comparison to values from experimental results and the most accurate values are obtained for average value of 3.07 W/m.K which the presented results are based upon. The acquired result show great agreement with the experimental results provided by Gokaslan et al. (2022). Results are presented for different flow rates and heat fluxes applied on channel walls.

In Figure 4.1, temperature distribution results of all the flow rate and heat flux values in porous medium consisting of particles with 3.17mm diameters in accordance with analytical solution of the domain and given in equation (2.48), are presented.

In Figure 4.1, the x-axis represents the progress in φ- direction in degrees, versus obtained temperature values based on equation (2.48). As expected, aside from imposed heat flux and minor inlet temperature differences between various tested models, best performance regarding the temperature increase is in case with the lowest flow rate, while lowest temperature increase is observed in case with highest flow rates. This matter is considered while analyzing critical factors affecting the overall heat transfer enhancement, and therefore is included as one of parameters in correlation-based equation (2.52) for temperature estimations.

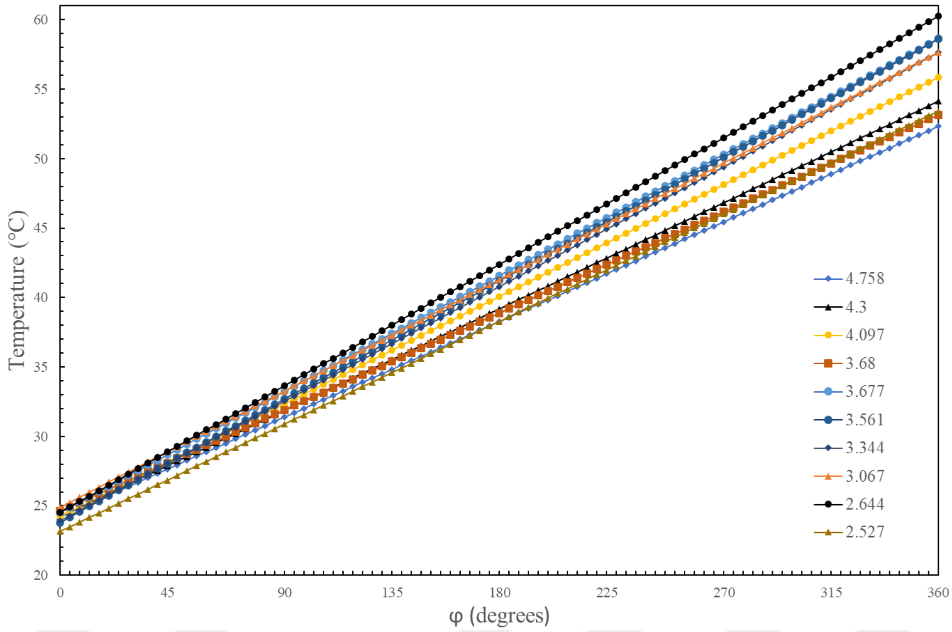

Figure 4.1: Temperature distribution results along channel based on analytical solution for different flow rates (g/s).

In order to emphasize on the effects of flow rate, temperature distribution of different flows with the same heat flux value of 266 W/m^2 are presented in Figure 4.2.

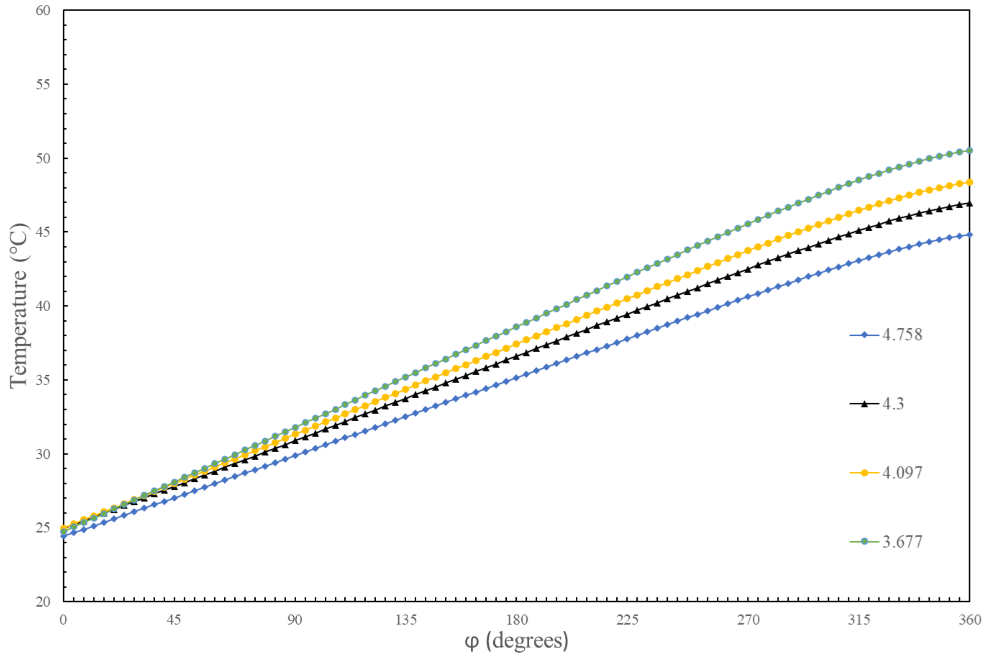

Figure 4.2: Temperature distribution along channel with imposed heat flux of 266 W/m^2 based on analytical solutions for different flow rates (g/s).

It can be clearly observed that the temperature increases within the channel being imposed to same thermal boundary conditions, solely depends on the flow rate of the inlet, with an opposite relation.

The accuracy of the solution and comparison based on experimental data will be done in Section 4 of Chapter 4.

4.2 COMSOL Simulation Results

Results based on COMSOL Multiphysics simulations, are presented with the same classifications applied on analytical solution. First, all the obtained results for all the flow rates and heat fluxes will be presented in Figure 4.3.

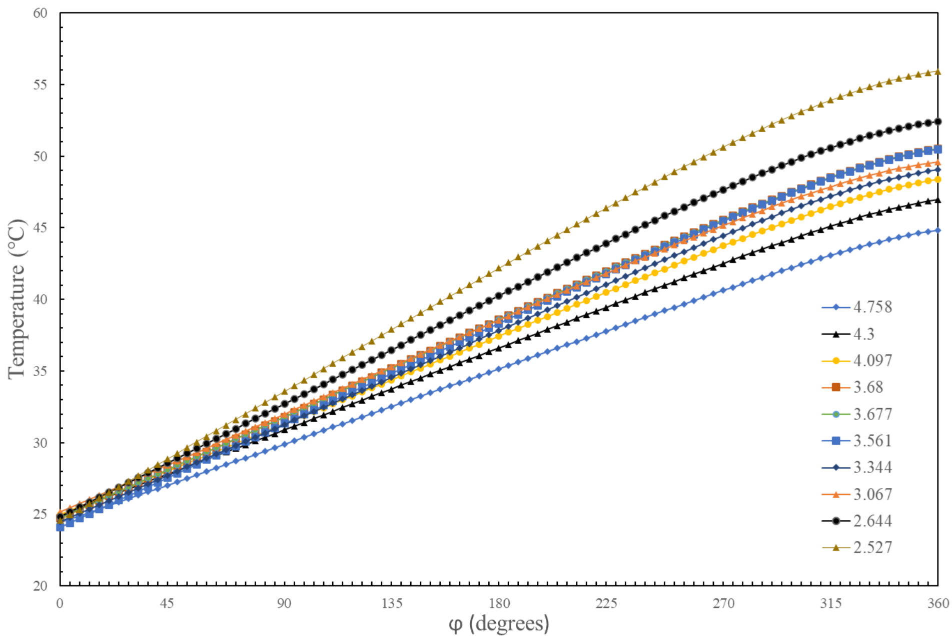

Figure 4.3: Temperature distribution along the channel obtained from COMSOL simulations for different flow rates (g/s).

In order to be able to compare the data obtained from all different methods, same conditions as in Figure 4.2 is considered for results of simulation from COMSOL and presented in Figure 4.4. All the presented flows have been imposed to the constant wall heat flux BC with the value of 266 W/m^2.

As a major difference from analytical solutions, in COMSOL simulations the temperature increase is not completely linear, and similarity to experimental data is observed as presented in Figures 4.3 and 4.5.

It is observed on Figure 4.4 that except from values of the simulation with 3.67 g/s flow rate, all other values confirm the prior assumptions made for the results obtained from analytical solutions regarding opposite relations between flow rate values and overall temperature increase along the channel.

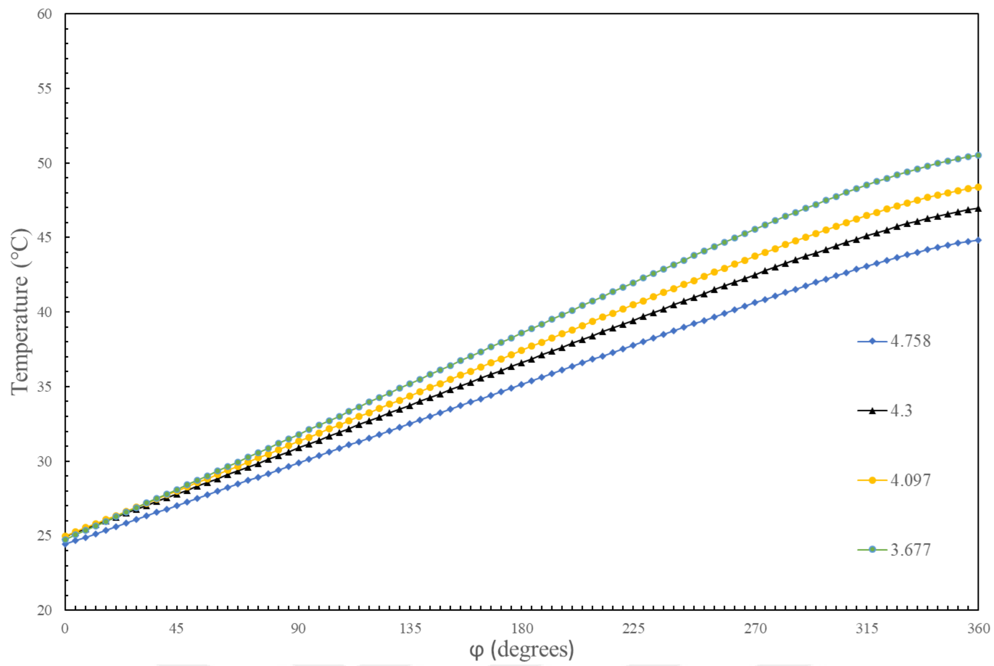

Figure 4.4: Temperature distribution along channel with imposed heat flux of 266 W/m^2 based on COMSOL simulations for different flow rates (g/s).

4.3 Correlation Based Results

As the main contribution, a correlation presented in equation (2.52) were obtained to be able to approximately understand temperature distribution along the channel without any dependency on experimental values as initial conditions. The values obtained by this method are presented in Figures 4.5 and 4.6 for all the flow rates and imposed heat flux values, and for different flow rates imposed to a constant heat flux of 266 W/m^2, as previously applied for results of other methods.

Results obtained from correlation-based equation follow the temperature and flow rate increase relation pattern, and as visible in Figures 4.5 and 4.6, the temperature increase in linear and opposite to flow rate changes.

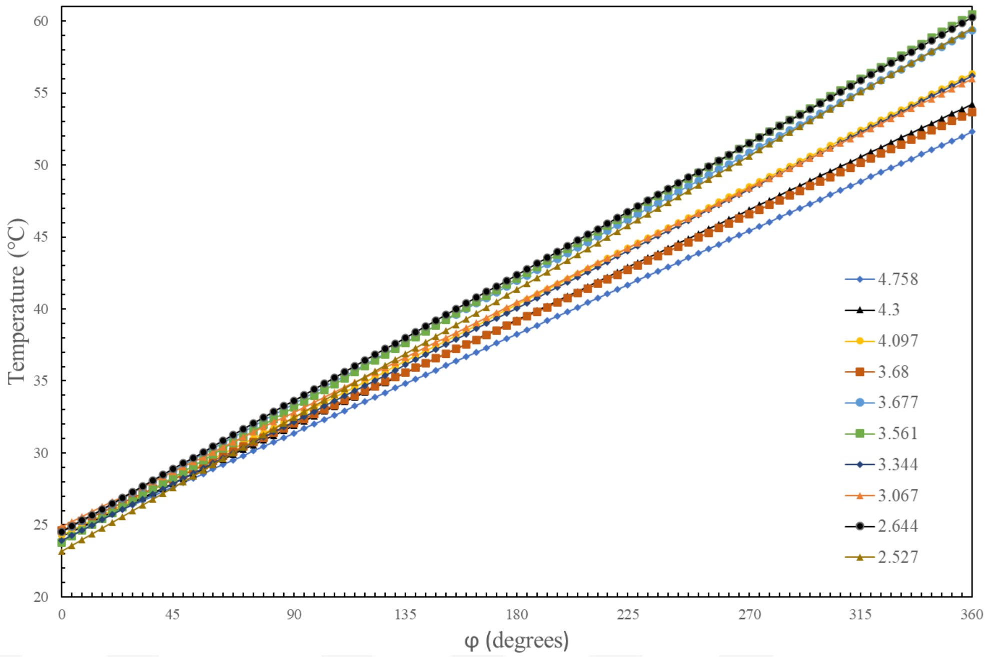

Figure 4.5: Temperature distribution along the channel obtained from proposed correlation-based equation over the domain for different flow rates (g/s).

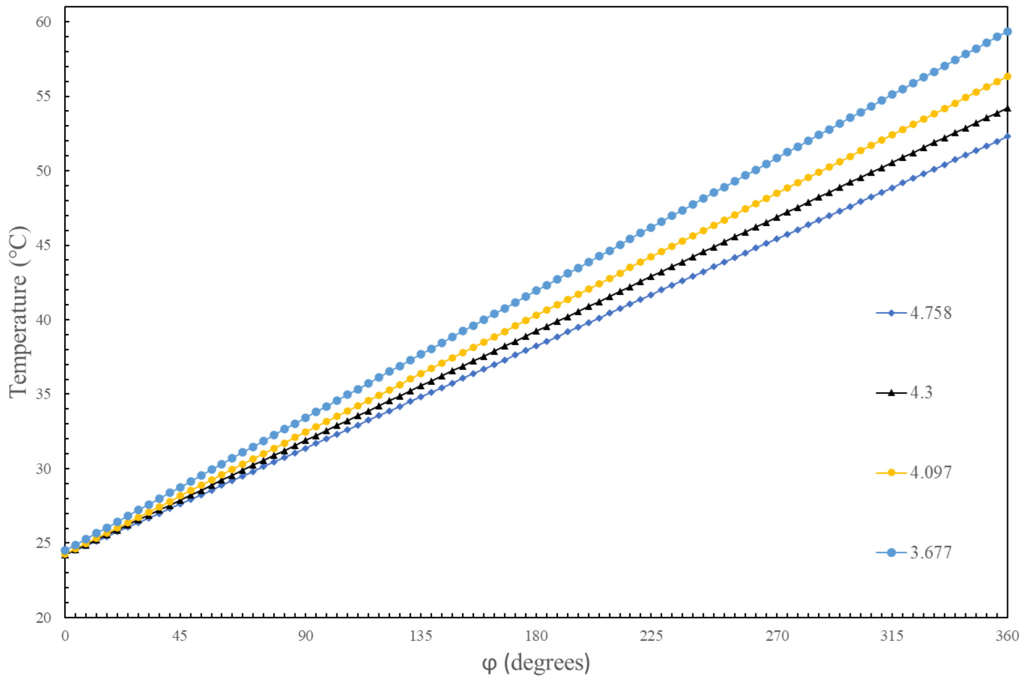

Figure 4.6: Temperature distribution along channel with imposed constant heat flux of 266 W/m2 obtained from proposed correlation-based equation over the domain for different flow rates (g/s).

4.4 Method Verification Vs. Experimental Data

While all the sample results from the data evaluated by different methods have been presented in the sections 1-3 of current chapter, accuracy of the methods, especially the proposed solutions must be evaluated in order to accept the validity of equations (2.48) and (2.52).

For this purpose, temperature distribution along the channel for all applied methods is presented separately, according to the inlet flow rate values. Figures 4.7 to 4.9 display these comparison graphs for flow rates of 4.75 g/s, 4.3 g/s and 3.68 g/s respectively. Graphs for other flow rates applied and evaluated are presented in Appendix B.

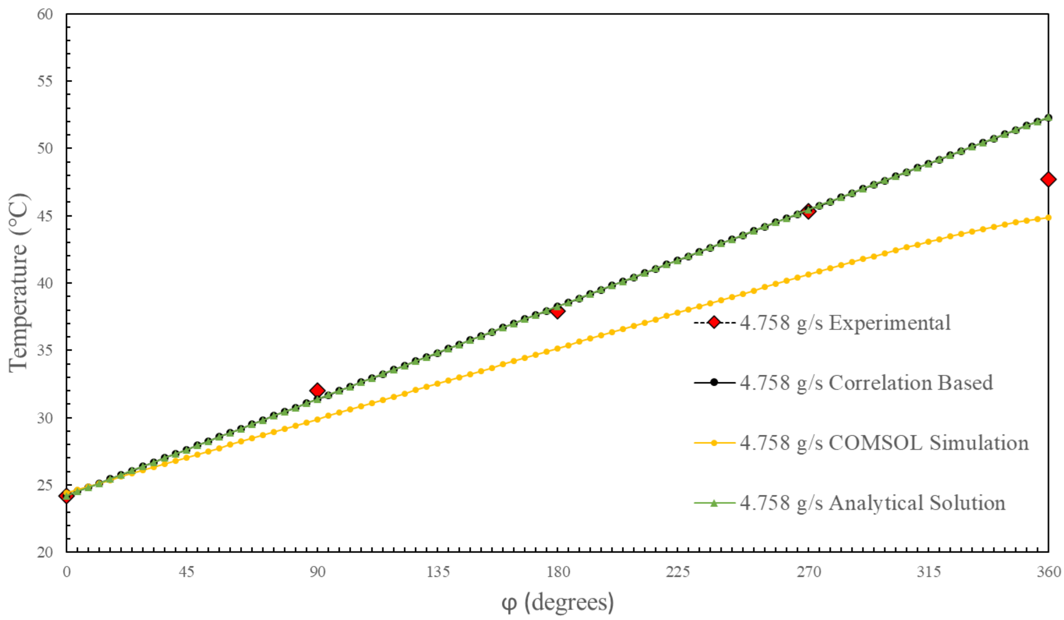

Figure 4.7: Temperature distribution comparison along channel between all applied methods and experimental data for 4.75 g/s flow rate.

Based on the temperature distribution values provided in Figures 4.7 to 4.9, it is seen that COMSOL simulation takes into consideration the heat losses in end of the channel and the profile are not linear as in analytical solution and correlation-based results. This difference in analytical and correlation-based solutions are a result of simplifying the geometry as cylindrical and used assumptions to solve the conservation equations.

Furthermore, COMSOL simulation results have evaluated the domain completely and obtained the closest profile to experimental data, considering the heat loss on end of the channel.

Considering the results for analytical solution and correlation-based equation in Figures 4.7 to 4.9, a good agreement in values along the channel is observed except the channel exit which is due to linear profile of the mentioned solutions and therefore, in further evaluations, only values up to 270 degrees along the channel considered.

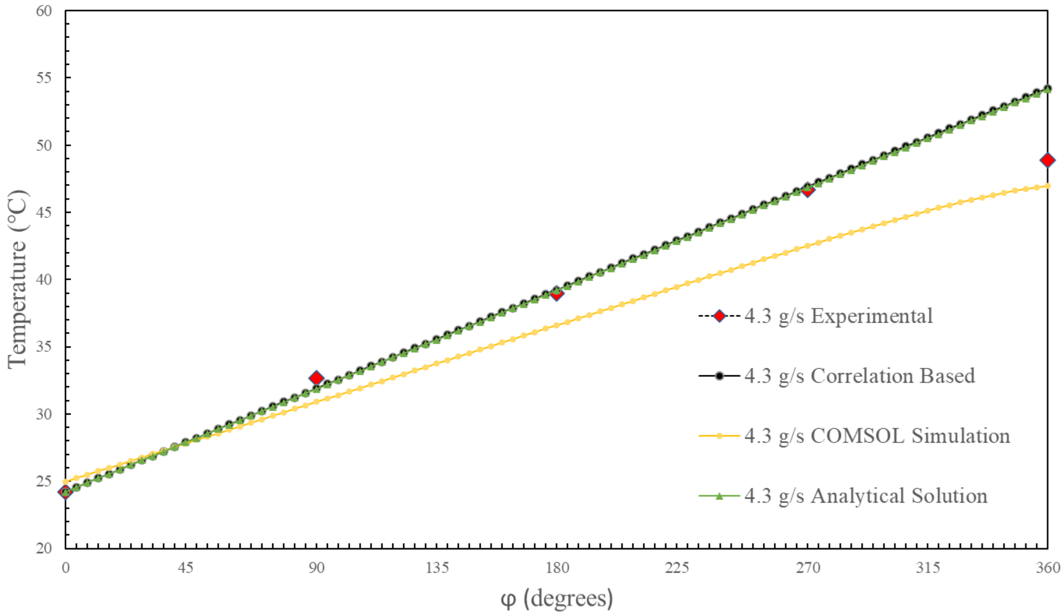

Figure 4.8: Temperature distribution comparison along channel between all applied methods and experimental data for 4.3 g/s flow rate.

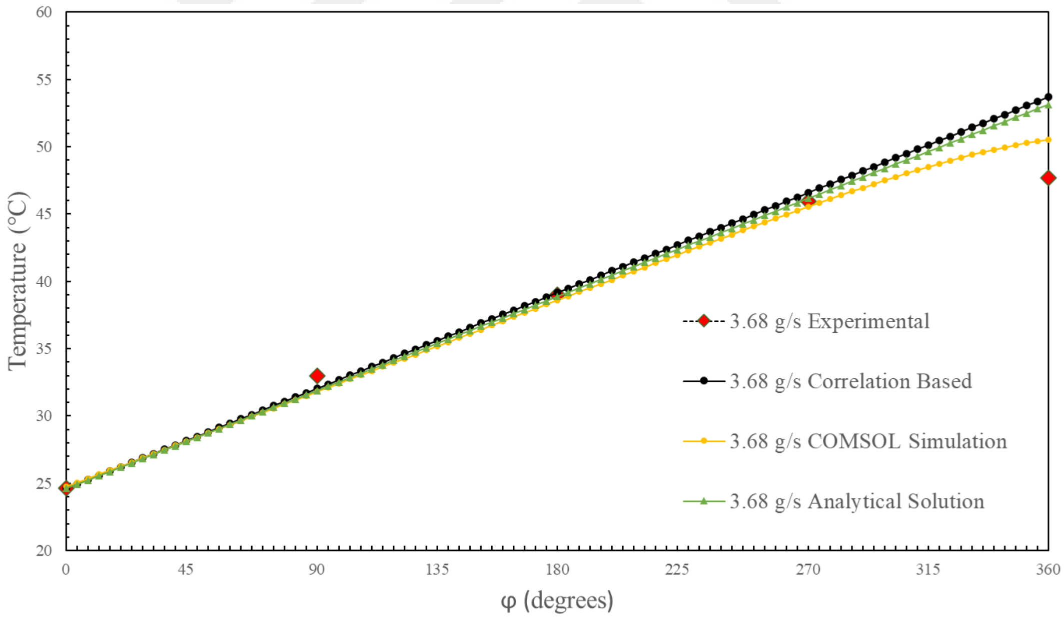

Figure 4.9: Temperature distribution comparison along channel between all applied methods and experimental data for 3.68 g/s flow rate.

To have a numerical understanding of the result accuracy of analytical solution and correlation-based equation, maximum error in calculated temperature values between 0 to 270 degrees along the channel is compared against values obtained from experimental setup by Gokaslan (2022) in Table 4.1. According to calculated values, maximum error value for analytical solution is %6.1 which is obtained in both lowest evaluated flow rate and Re_{dh}. It can be interpreted from the Table 4.1 that as Re_{dh} increases, solution accuracy increases relatively.

Table 4.1: Maximum error value for temperature distribution of analytical solution.

Flow Rate (g/s)	Re_{dh}	Experimental C_T	Maximum Error
2.644	1132.52	5.68	%6.1
3.067	1300.11	5.22	%4.6
3.344	1394.23	5.36	%4.3
3.561	1482.38	5.53	%3.3
3.677	1564.19	5.43	%3.5
3.68	1582.23	4.54	%3.3
4.097	1721.63	5.02	%2.3
4.3	1873.98	4.75	%2.3
4.758	1995.58	4.47	%1.9

For correlation-based equation of (2.52), error values of calculated temperature distribution versus experimental data of Gokaslan (2022) is presented in Table 4.2.

Table 4.2: Maximum error value for temperature distribution of correlation-based equation.

Flow Rate (g/s)	Re_{dh}	Correlated C_T	Maximum Error
2.644	1132.52	5.68	%6.1
3.067	1300.11	4.94	%5.8
3.344	1394.23	5.13	%5.4
3.561	1482.38	5.83	%1.9
3.677	1564.19	5.54	%2.9
3.68	1582.23	4.62	%2.9
4.097	1721.63	5.10	%2.3
4.3	1873.98	4.77	%2.3
4.758	1995.58	4.47	%2

Considering the calculated values in Table 4.2, the maximum error value of the results provided by correlation-based equation of (2.52) is %6.1 versus experimental data. Linear relation of increase in Re_{dh} and solution accuracy, is also valid for correlated-based equation of (2.52). As obtained results from equation (2.52) and error values presented in Table 4.2 are considered, it is verified that as flow rate and Re_{dh} grow higher, analytic assumptions and obtained solutions get closer to the actual condition and therefore, obtained values from experimental setup by Gokaslan (2022).

Table 4.3: Error value of correlated base C_T in comparison to experimental data.

Flow Rate (g/s)	Re_{dh}	Experimental C_T	Correlated base C_T	Error
2.644	1132.52	5.68	5.68	%0
3.067	1300.11	5.22	4.94	%5.20
3.344	1394.23	5.36	5.13	%4.30
3.561	1482.38	5.53	5.83	%5.35
3.677	1564.19	5.43	5.54	%2.15
3.68	1582.23	4.54	4.62	%1.94
4.097	1721.63	5.02	5.10	%1.53
4.3	1873.98	4.75	4.77	%0.32
4.758	1995.58	4.47	4.47	%0.12

While the results require more work subject to a wider range of Re_{dh}, based on the results and comparison made, both analytical solutions provided in equation (2.48) and correlation-based temperature equation (2.52) are considered acceptable for calculations in packed bed spiral heat exchangers subject to the constant heat flux on the walls BC filled with steel balls.

4.5 Conclusion

Data verification step with experimental results have proven validity of the analytical solution and the correlation-based equation for temperature distribution along the channel up to 270 degrees, since they follow a linear profile due to the applied simplifications and assumptions made, and do not consider the heat loss effects on end of the channel which has a significant impact on the corresponding values as it can be seen from the experimental results. Despite all the mentioned simplifications applied while acquiring the analytical solution, results obtained from both analytical and correlation-based equations have only maximum error value of %6.1 versus experimental results, which is obtained on the lowest flow rate and Re_{dh} values. It is observed that the accuracy of both analytical solution and correlation-based equation, increases in accordance to increase in the flow rate and Re_{dh} values, and therefore the error value is at its minimum on the highest flow rate that was experimentally tested.

Simulation results obtained on COMSOL Multiphysics show a similar profile and temperature distribution pattern to the experimental results, and contrary to analytical solution, do not have a linear profile. The precision of this simulation is high on the temperature values of the channel exit and similar to results obtained in the experiments. On the other hand, along the channel, the precision is extremely low and do not provide reliable results.

Future work of this study is to evaluate accuracy of the analytical solution and correlation-based equations against the experimental results of straight channels, as both empty and filled with steel balls or other types of porous medium. Furthermore, corresponding values for thermal dispersion conductivity must be investigated more thoroughly and in details for the most accurate values along the channel.

REFERENCES

Agus Pulung Sasmito, J. C. (2011). Numerical evaluation of laminar heat transfer enhancement in nanofluid flow in coiled square tubes. *Nanoscale Research Letters*.

Awad, M. (2010). Heat Transfer for Laminar Thermally Developing Flow in Parallel-Plates Using the Asymptotic Method. Cairo, Egypt: IEEE.

C. T. Hsu, P. Cheng. (1990). Thermal Dispersion in Porous medium. *International Journal of heat and mass transfer*, 1587-1597.

Crane & Vachon. (1977). A prediction of the bounds on the effective thermal conductivity of granular materials. *International Journal of Heat and Mass Transfer, 20*(7), 711-723.

Donald A. Nield, A. B. (2017). *Convection in Porous Media.*

Ergun, S. (1952). Fluid Flow Through Packed Columns. *Chemical Engineering Progress*, 89-94.

H.J. Xu, L. G. (2015). Analytical considerations of local thermal non-equilibrium conditions for thermal transport in metal foams. *International Journal of Thermal Sciences*.

Hadley, G. (1986). Thermal Conductivity of Packed Metal Powders. *Int. J. of Heat and Mass Transfer*, 909-920.

Hersman, S., Hu, K., Hunter, B., Sunday, D., Yang, L. (2006). Flow Through Packed Beds: Investigation of the Ergun Equation and Development of a Straw Model of Packed Beds. *Transport Processes Laboratory*, 363.

Johnson, J. B. (1975). Direct Contact Heat Transfer between two immiscible liquids in laminar flow between parallel plates.

Johnson, Jacobs, Boehm. (1975). Direct Contact Heat Transfer between two immiscible liquids in laminar flow between parallel plates.

K. Vafai, S. J. Kim. (1989). Forced Convection in a Channel Filled With a Porous Medium: An Exact Solution. *Journal of Heat Transfer*.

Kaviany, M. (2005). *Principles of Heat Transfer in POrous Media.*

M. Özdemir, A. F. Özgüç. (1997). Forced convective heat transfer in porous medium of wire screen meshes. *Heat and Mass Transfer*.

M.L.Hunt, C.L.Tien. (1988). Effects of thermal dispersion on forced convection in fibrous media. *International Journal of Heat and Mass Transfer*, 301-309.

Mustafa Yasin Gokaslan, Mustafa Ozdemir, Lütfullah Kuddusi. (2022). Experimental study on laminar air flow and heat transfer through a spiral channel filled with steel balls. *International Journal of Thermal Sciences*.

Sk Zeeshan Ali, a. S. (2019). Hydrodynamics of a weakly curved channel. *Physics of Fluids*.

Whitaker, S. (1973). The transport equations for multi-phase systems. *Chem. Eng. Sci 28*, 139-147.

APPENDICES

APPENDIX A: COMSOL MULTIPHYSICS Simulation Results
APPENDIX B: Results for all applied methods based on flow rates

APPENDIX A

This Appendix includes all output data containing heat transfer analysis (temperature distribution) and hydrodynamical analysis (velocity and pressure distribution) within the domain from each COMSOL Simulation for corresponding flow rates.

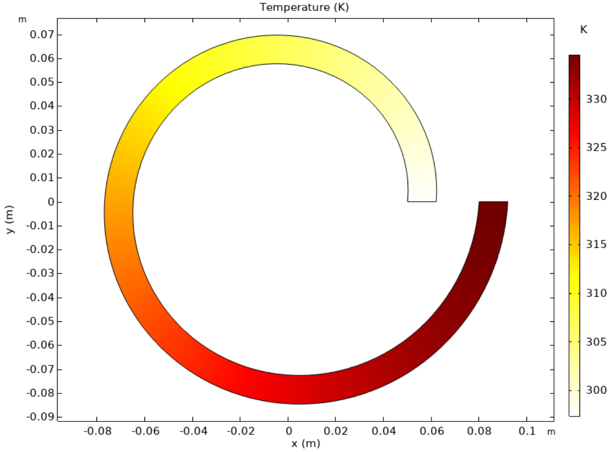

(a) Temperature Distribution

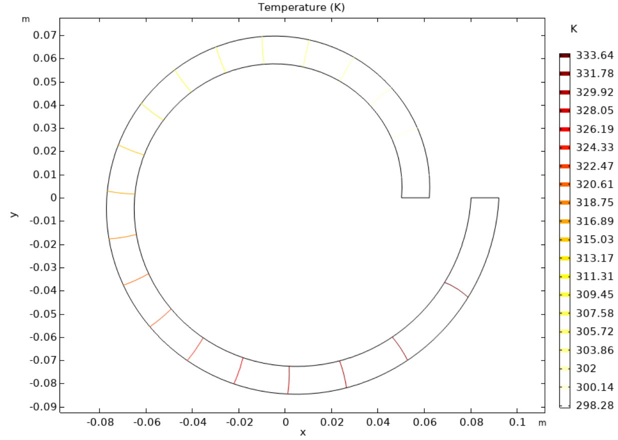

(b) Isothermal Contour

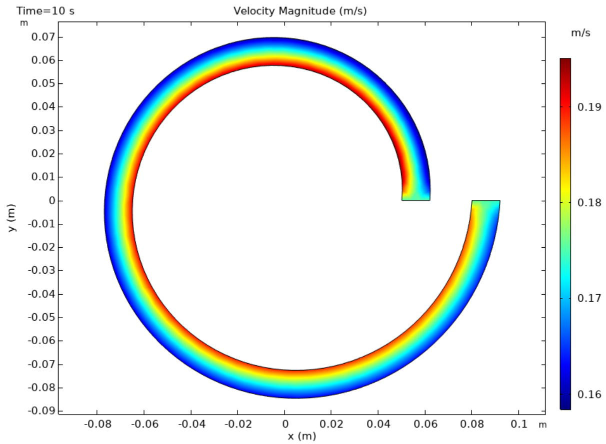

(c) Velocity Magnitude

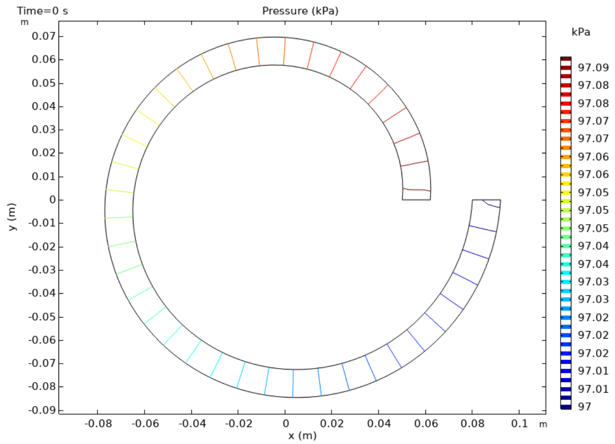

(d) Pressure Contour

Figure A.1: COMSOL Simulation results for 2.1 g/s flow rate

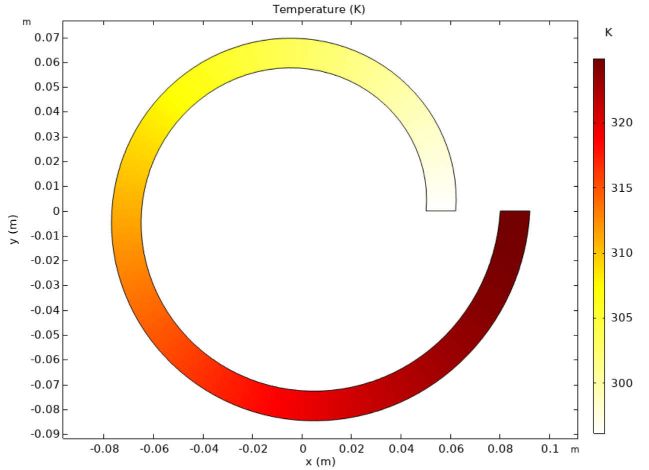

(a) Temperature Distribution

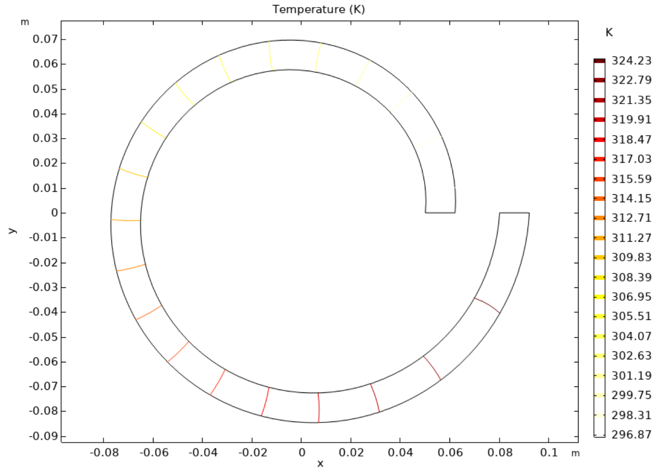

(b) Isothermal Contour

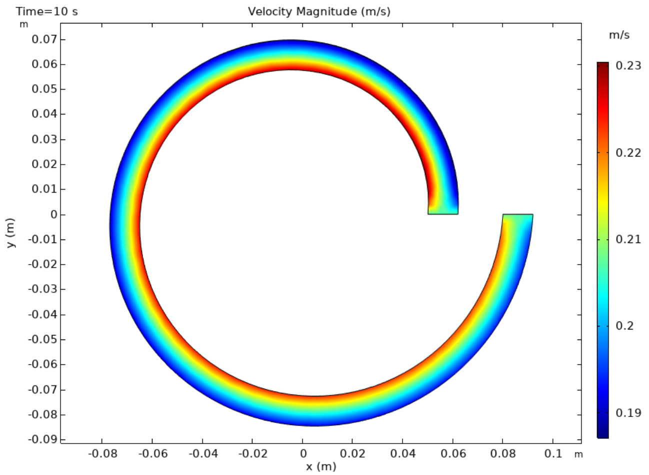

(c) Velocity Magnitude

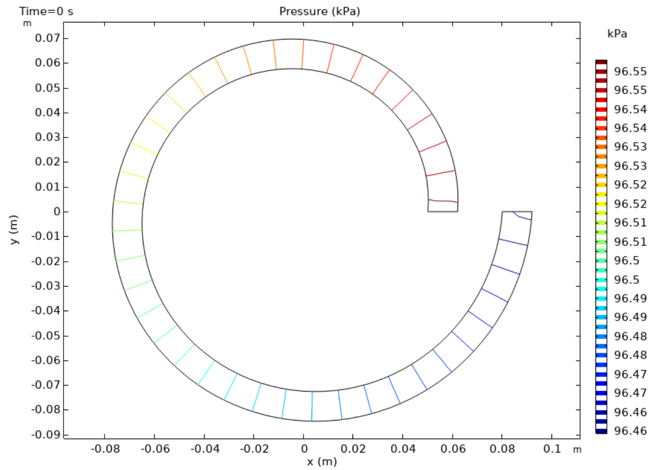

(d) Pressure Contour

Figure A.2: COMSOL Simulation results for 2.498 g/s flow rate

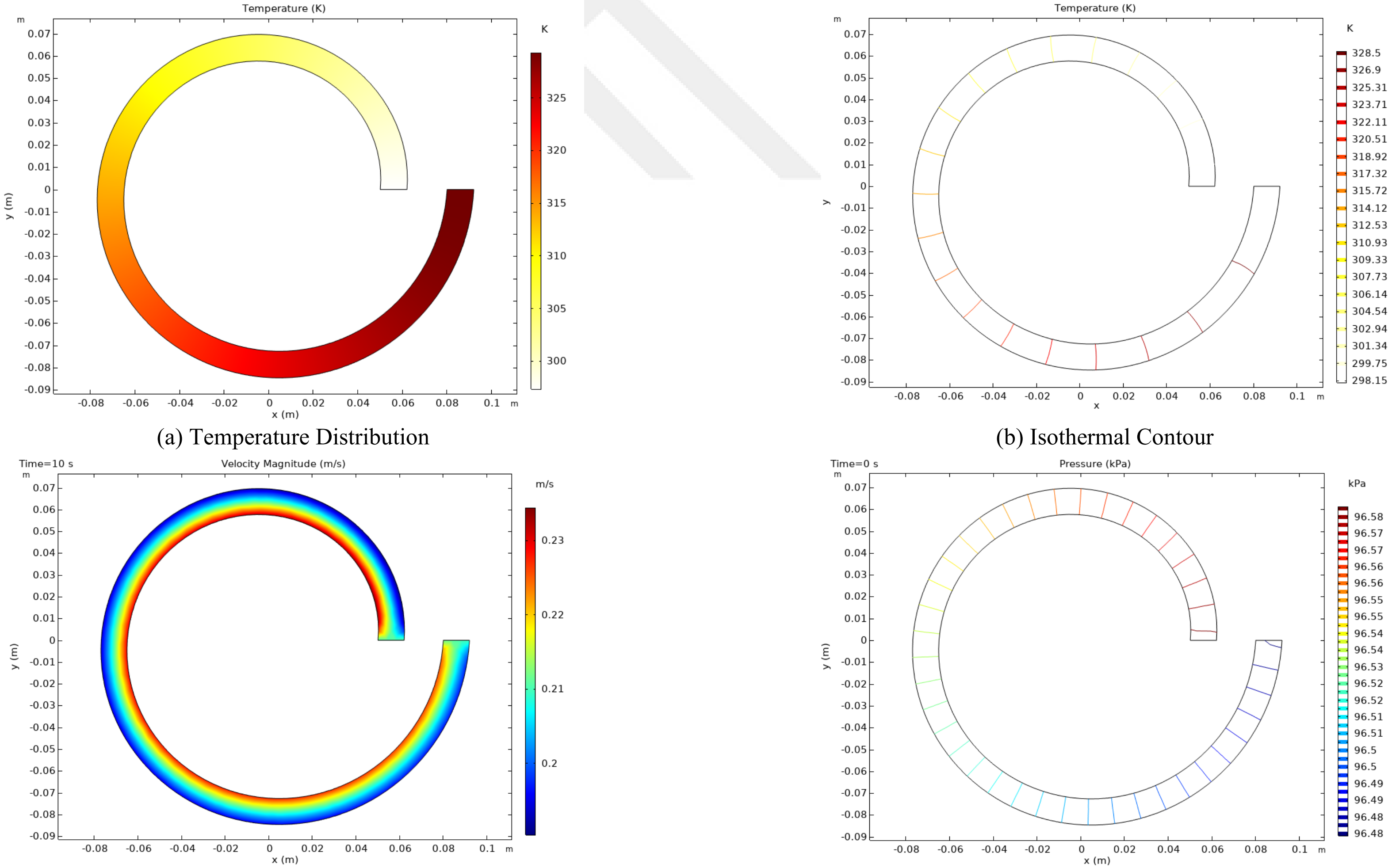

(a) Temperature Distribution

(b) Isothermal Contour

(c) Velocity Magnitude

(d) Pressure Contour

Figure A.3: COMSOL Simulation results for 2.527 g/s flow rate

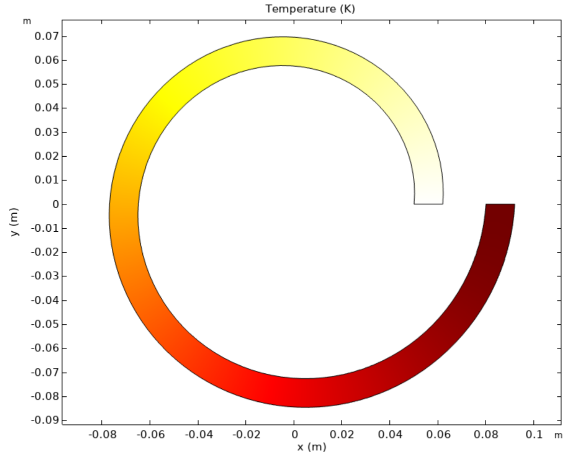

(a) Temperature Distribution

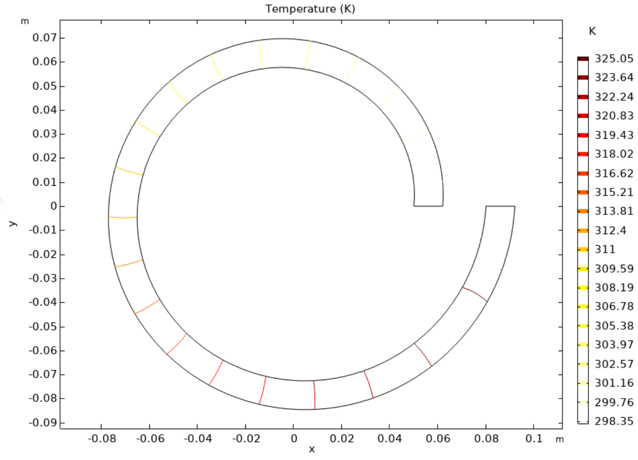

(b) Isothermal Contour

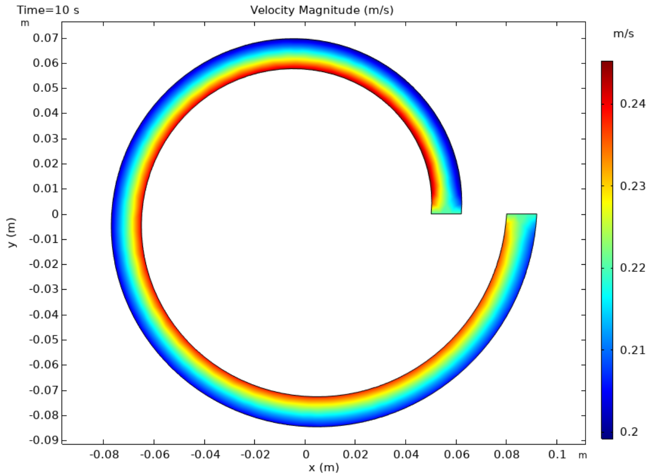

(c) Velocity Magnitude

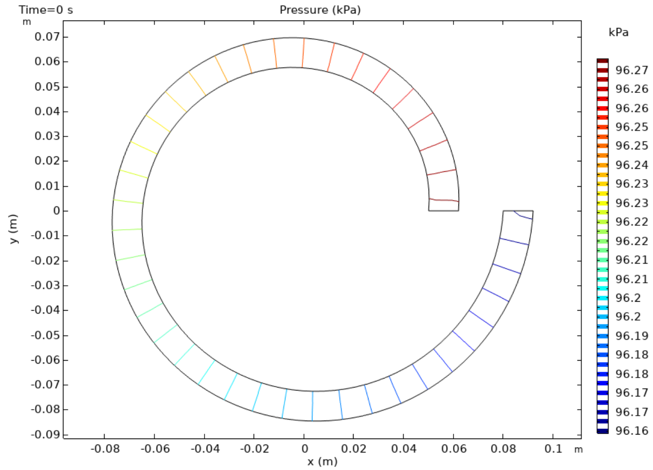

(d) Pressure Contour

Figure A.4: COMSOL Simulation results for 2.64 g/s flow rate

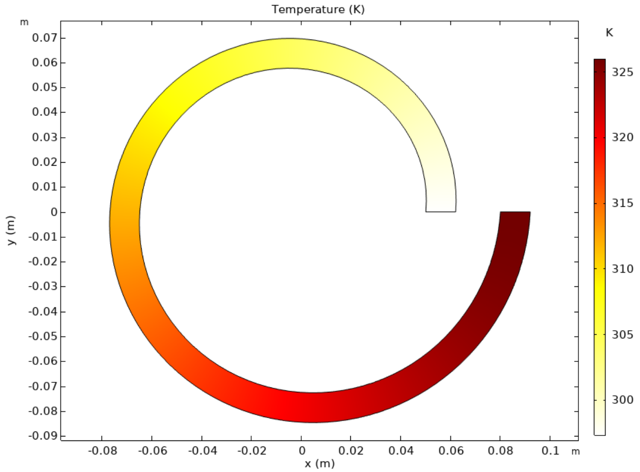

(a) Temperature Distribution

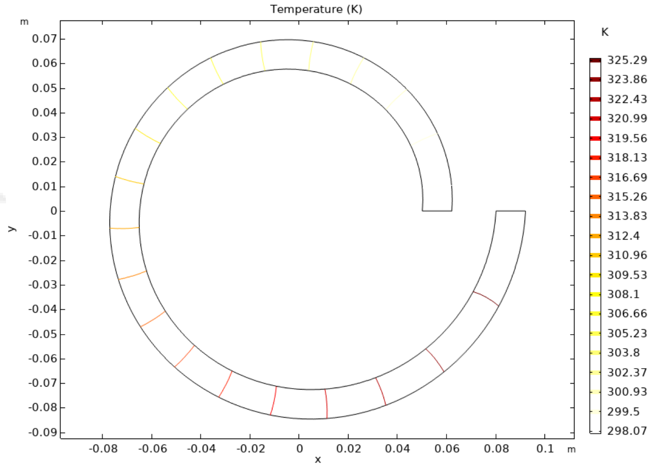

(b) Isothermal Contour

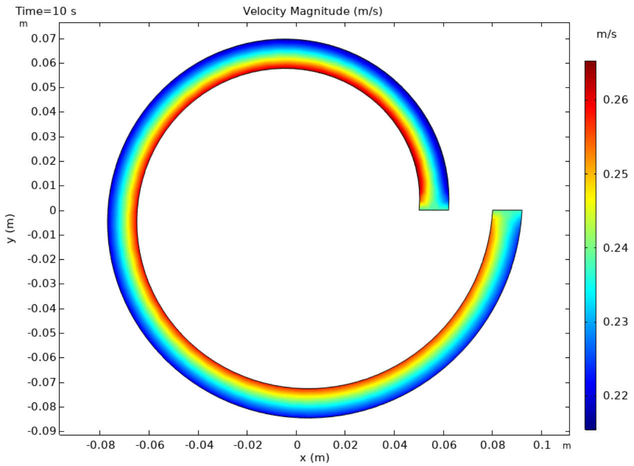

(c) Velocity Magnitude

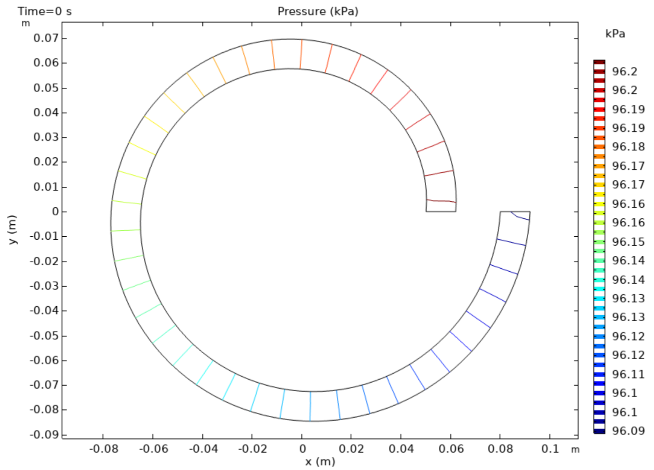

(d) Pressure Contour

Figure A.5: COMSOL Simulation results for 2.8 g/s flow rate

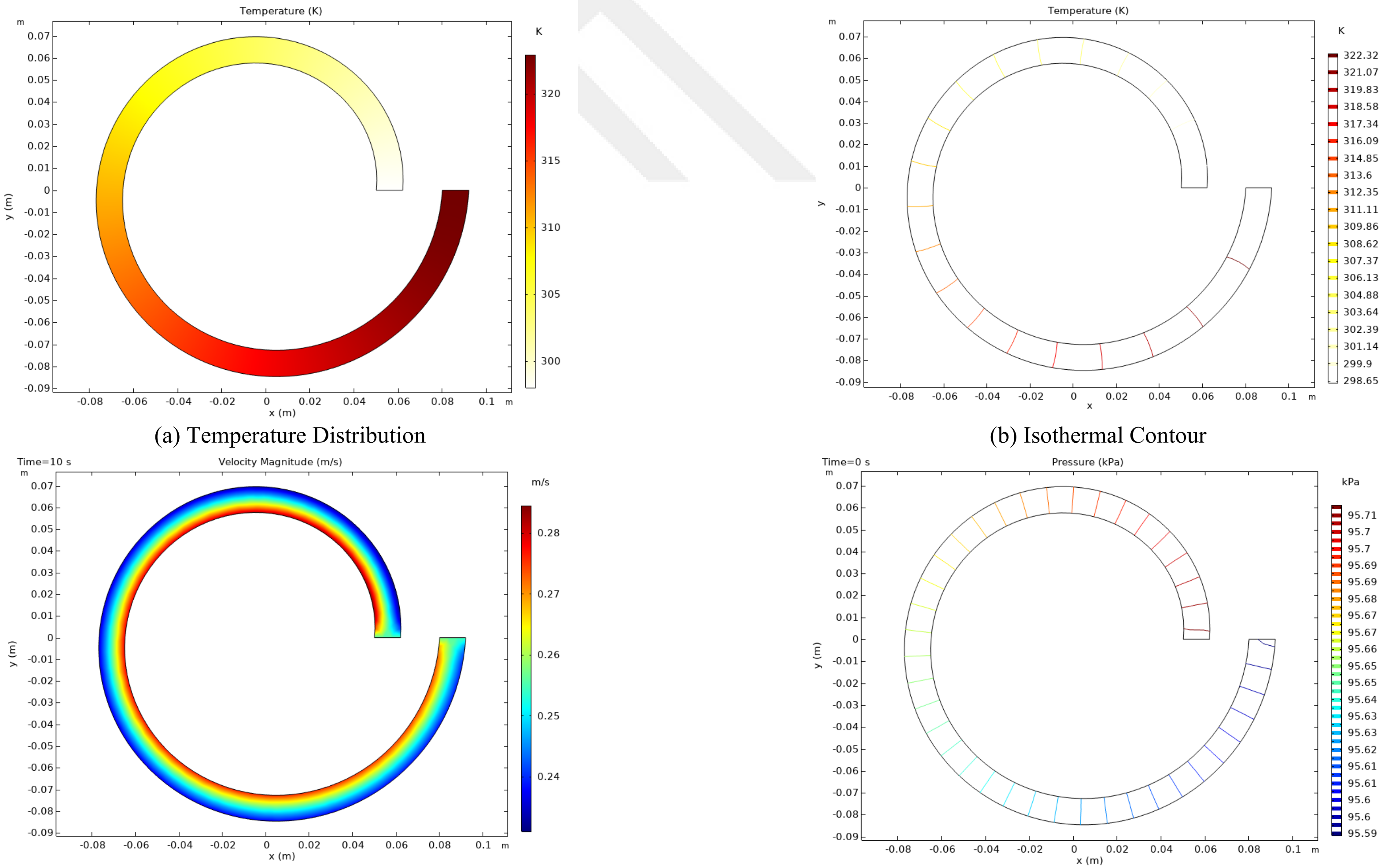

(a) Temperature Distribution

(b) Isothermal Contour

(c) Velocity Magnitude

(d) Pressure Contour

Figure A.6: COMSOL Simulation results for 3.067 g/s flow rate

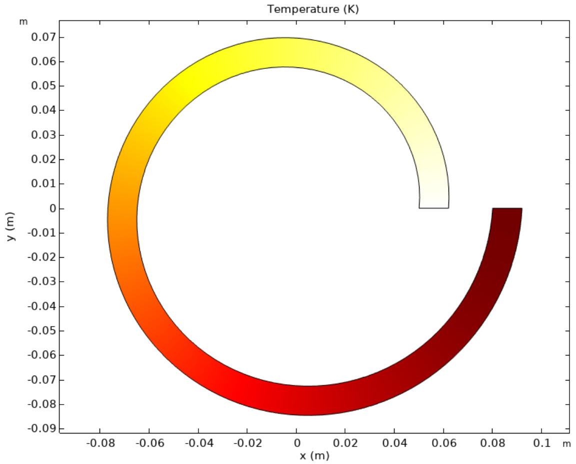

(a) Temperature Distribution

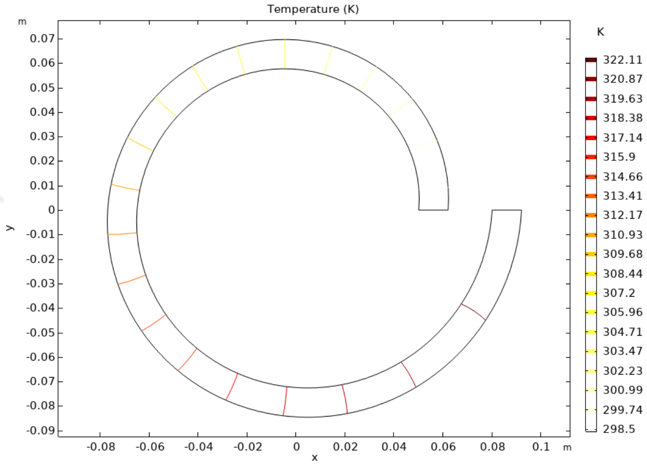

(b) Isothermal Contour

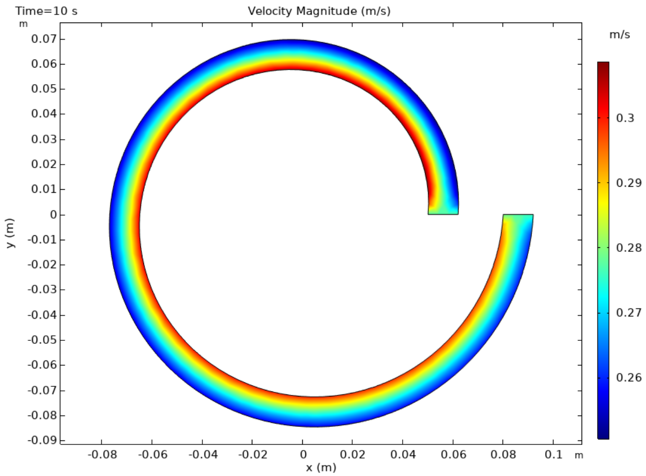

(c) Velocity Magnitude

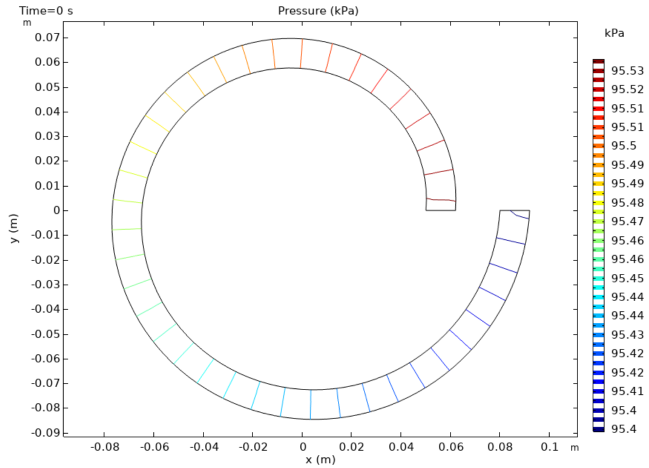

(d) Pressure Contour

Figure A.7: COMSOL Simulation results for 3.327 g/s flow rate

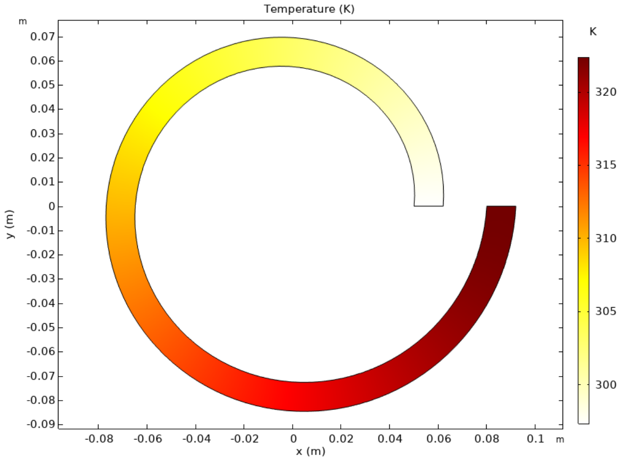

(a) Temperature Distribution

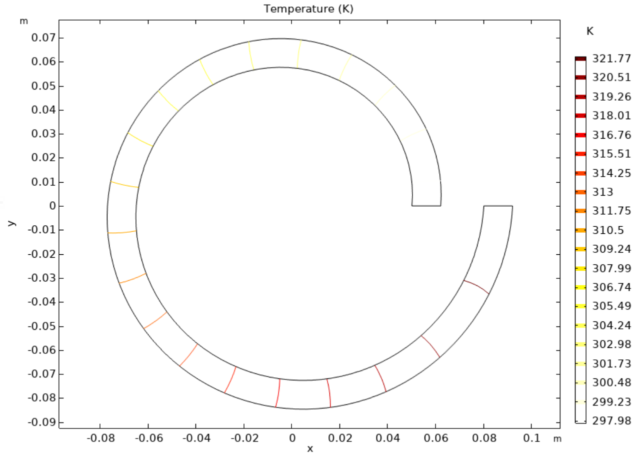

(b) Isothermal Contour

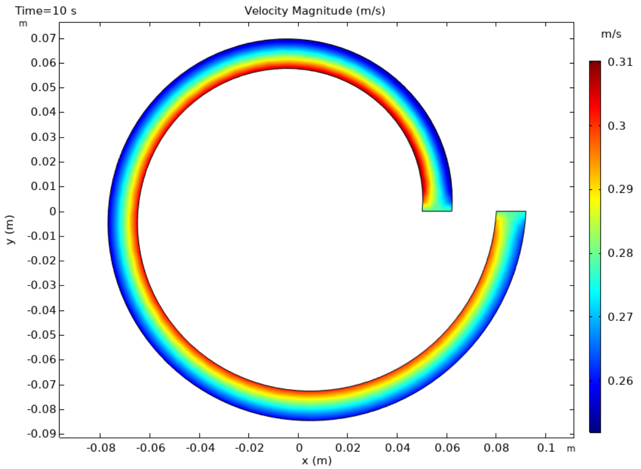

(c) Velocity Magnitude

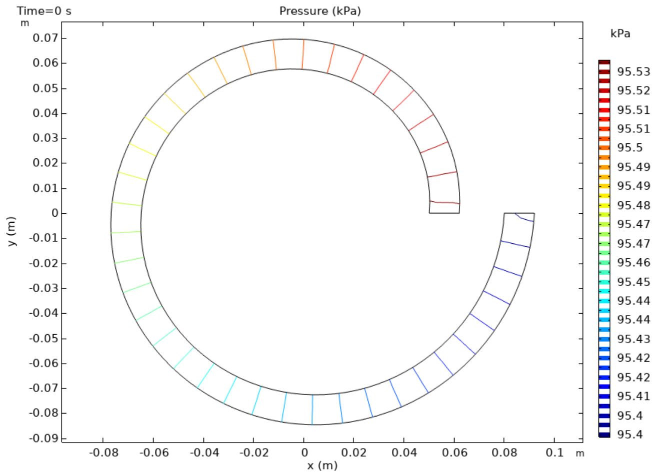

(d) Pressure Contour

Figure A.8: COMSOL Simulation results for 3.344 g/s flow rate

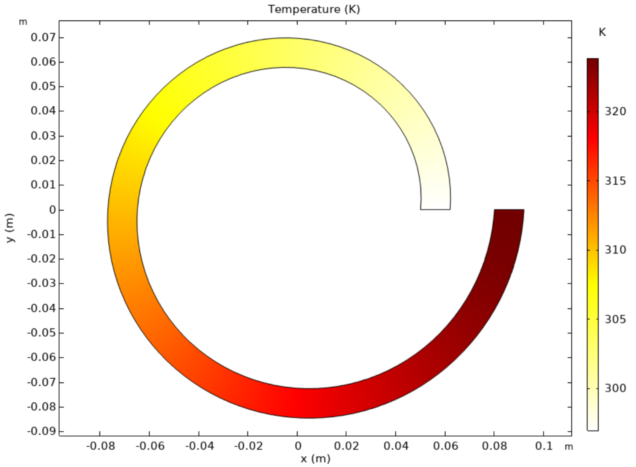

(a) Temperature Distribution

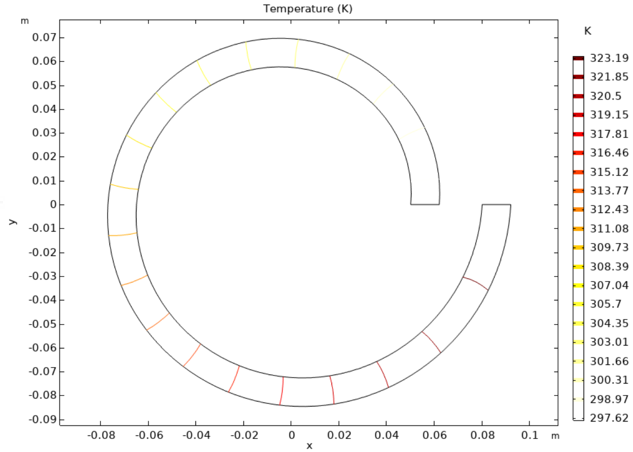

(b) Isothermal Contour

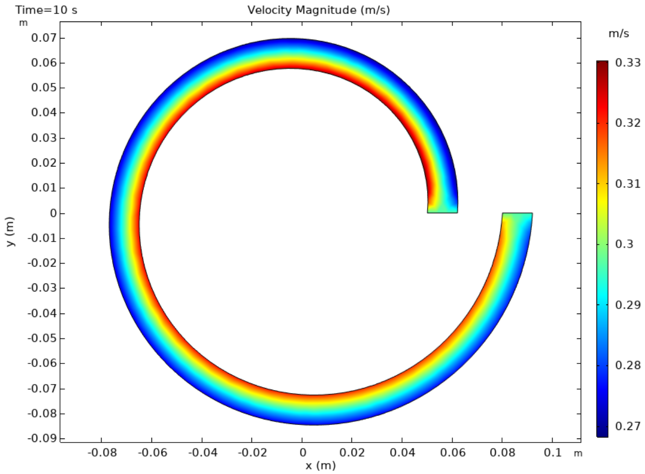

(c) Velocity Magnitude

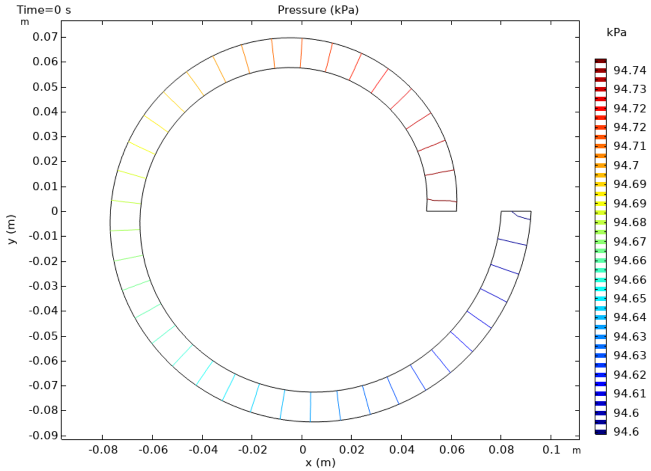

(d) Pressure Contour

Figure A.9: COMSOL Simulation results for 3.561 g/s flow rate

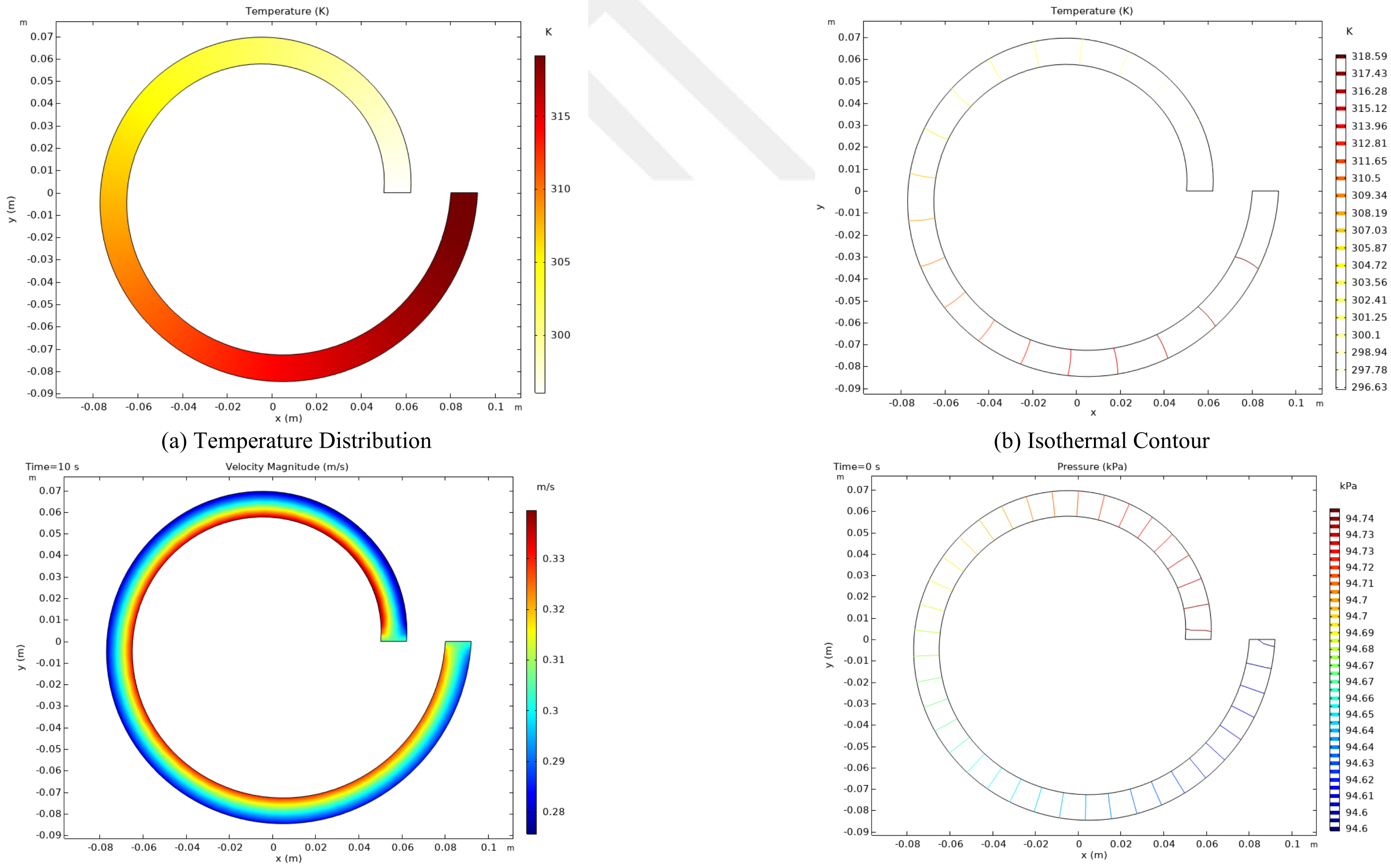

(a) Temperature Distribution

(b) Isothermal Contour

(c) Velocity Magnitude

(d) Pressure Contour

Figure A.10: COMSOL Simulation results for 3.66 g/s flow rate

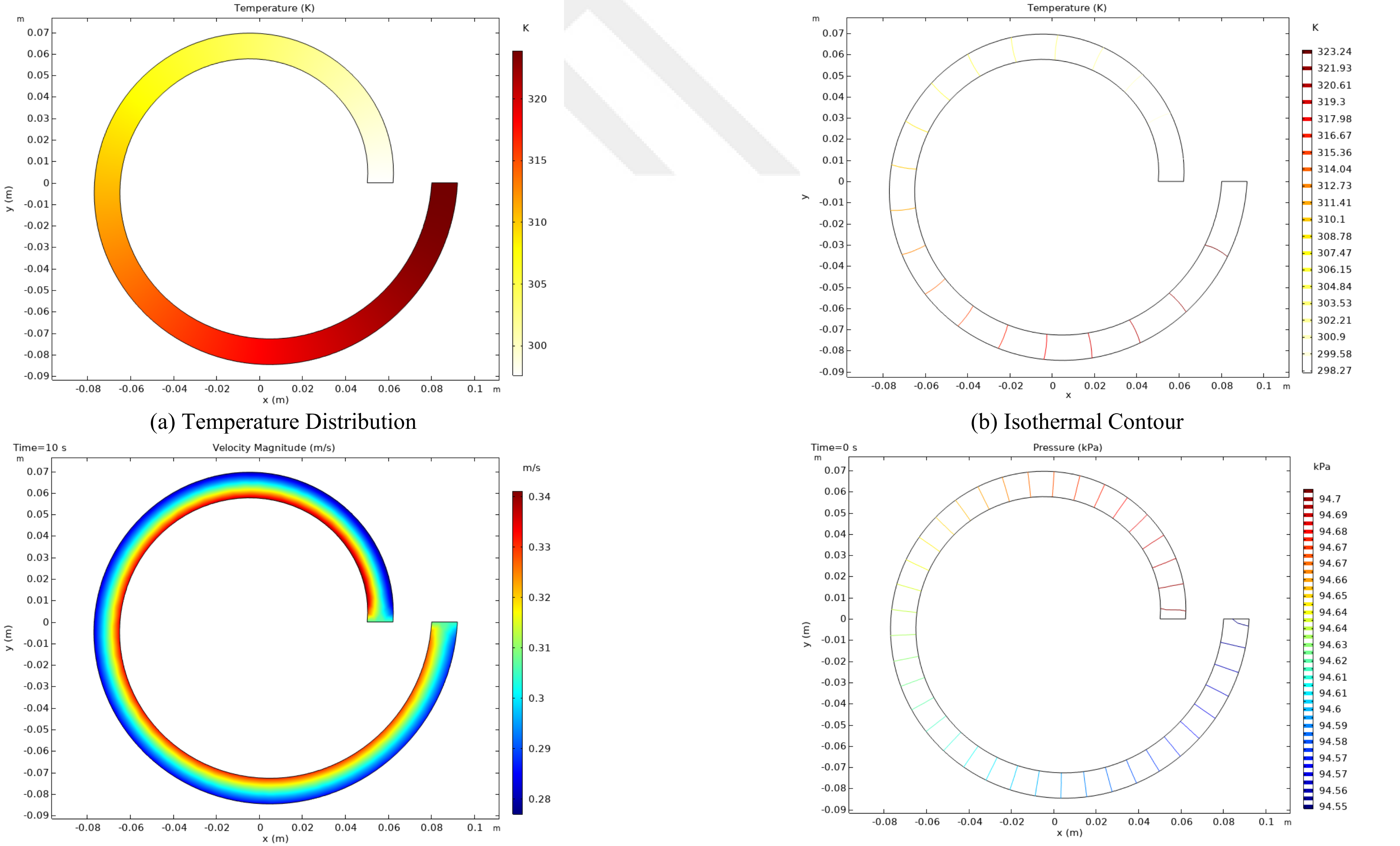

(a) Temperature Distribution

(b) Isothermal Contour

(c) Velocity Magnitude

(d) Pressure Contour

Figure A.11: COMSOL Simulation results for 3.677 g/s flow rate

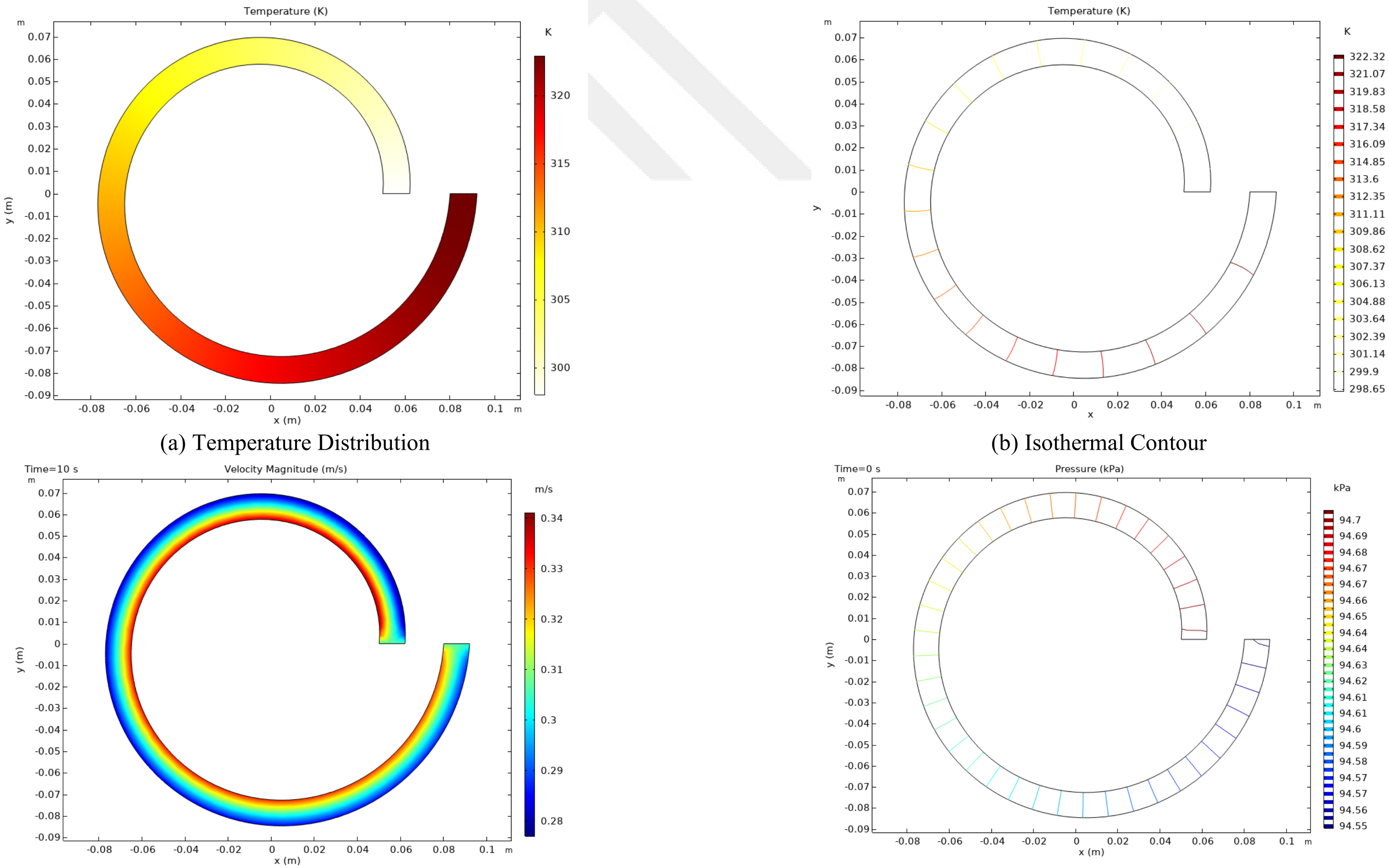

(a) Temperature Distribution

(b) Isothermal Contour

(c) Velocity Magnitude

(d) Pressure Contour

Figure A.12: COMSOL Simulation results for 3.68 g/s flow rate

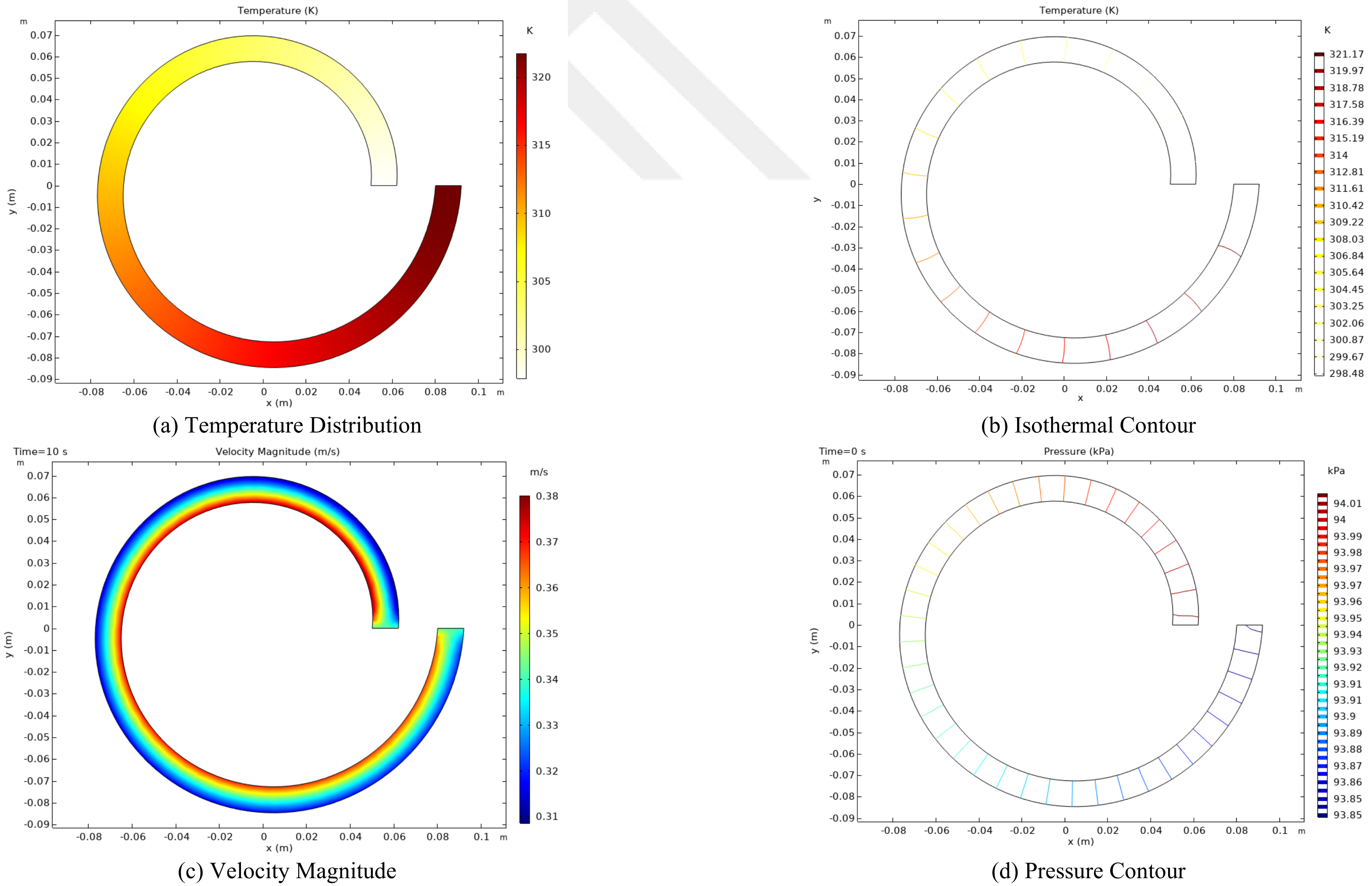

(a) Temperature Distribution

(b) Isothermal Contour

(c) Velocity Magnitude

(d) Pressure Contour

Figure A.13: COMSOL Simulation results for 4.097 g/s flow rate

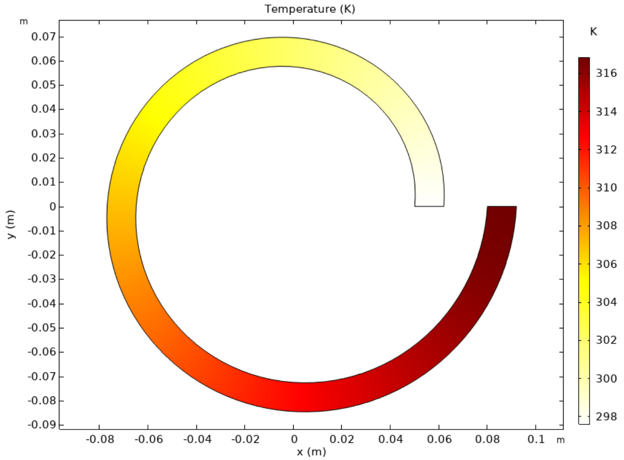

(a) Temperature Distribution

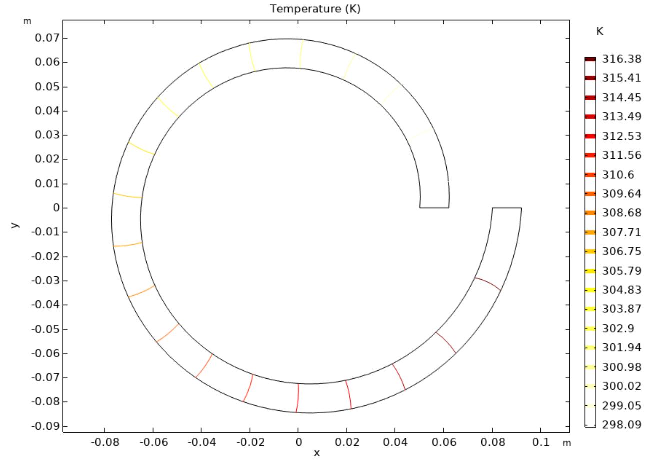

(b) Isothermal Contour

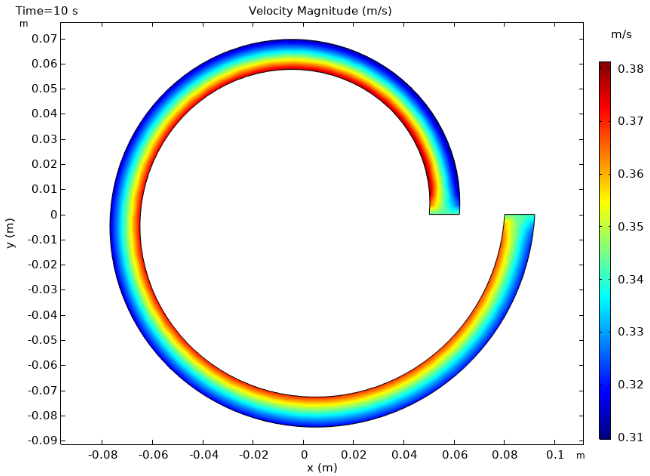

(c) Velocity Magnitude

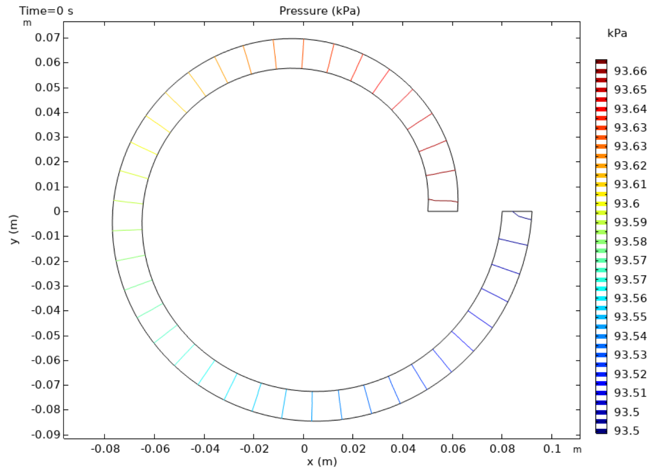

(d) Pressure Contour

Figure A.14: COMSOL Simulation results for 4.111 g/s flow rate

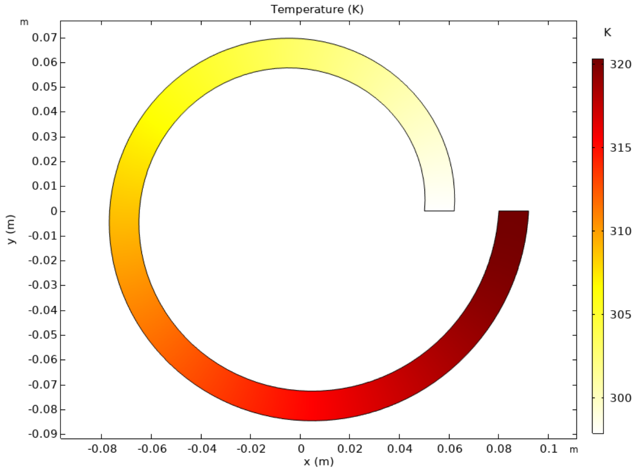

(a) Temperature Distribution

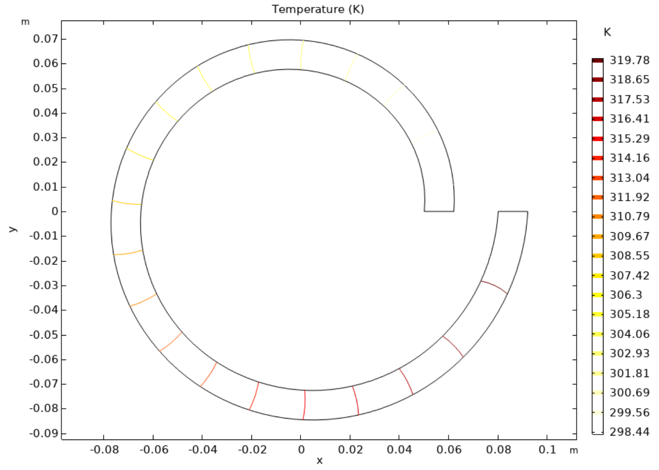

(b) Isothermal Contour

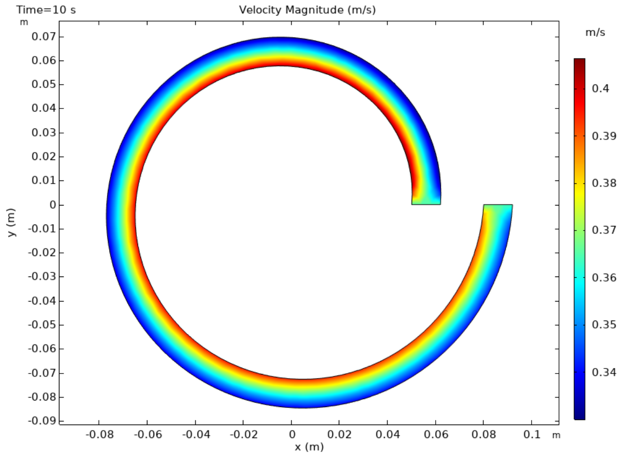

(c) Velocity Magnitude

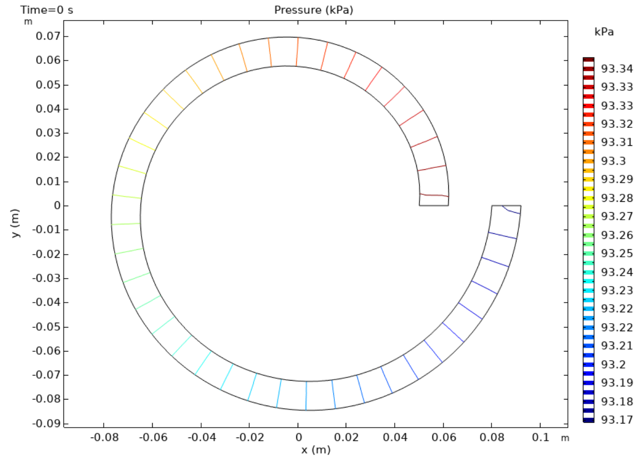

(d) Pressure Contour

Figure A.15: COMSOL Simulation results for 4.3 g/s flow rate

APPENDIX B

Results obtained from all applied methods for all the flow rates are presented here.

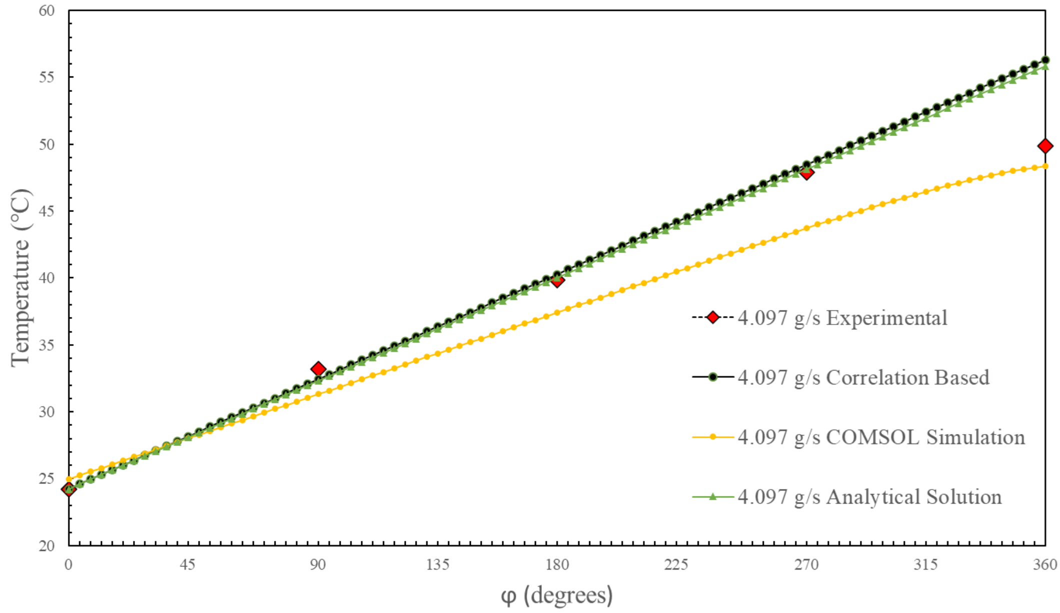

Figure B.1: Temperature distribution comparison along channel between all applied methods and experimental data for 4.097 g/s flow rate

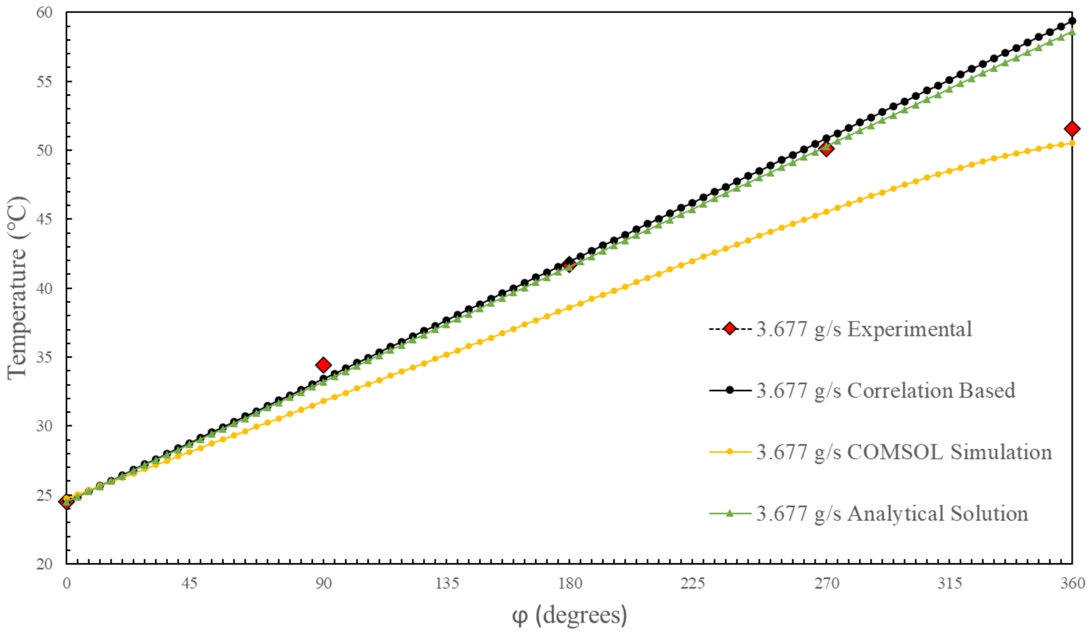

Figure B.2: Temperature distribution comparison along channel between all applied methods and experimental data for 3.677 g/s flow rate

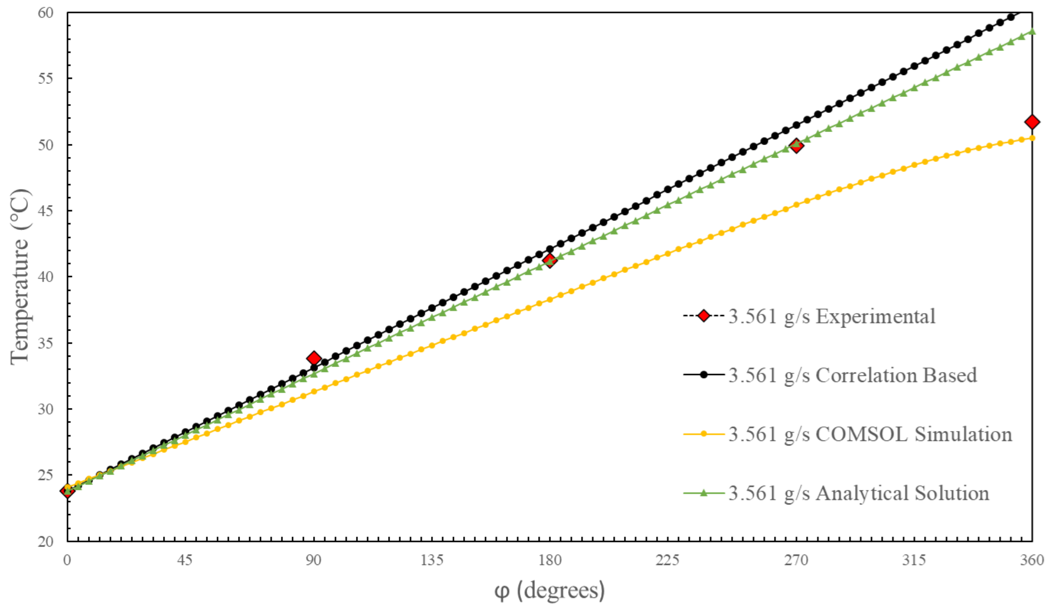

Figure B.3: Temperature distribution comparison along channel between all applied methods and experimental data for 3.561 g/s flow rate

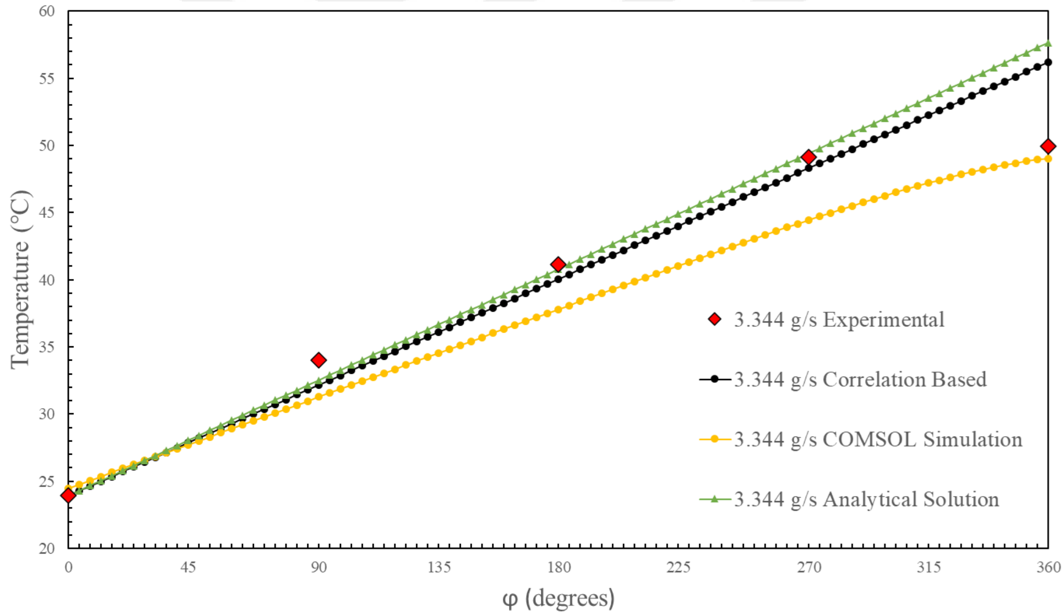

Figure B.4: Temperature distribution comparison along channel between all applied methods and experimental data for 3.344 g/s flow rate

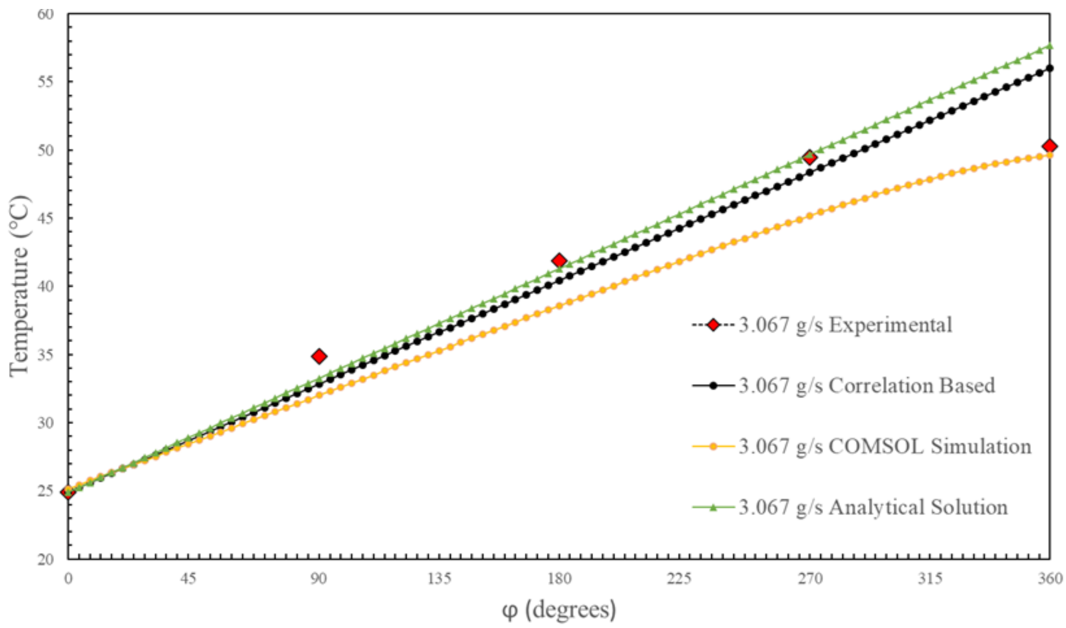

Figure B.5: Temperature distribution comparison along channel between all applied methods and experimental data for 3.067 g/s flow rate

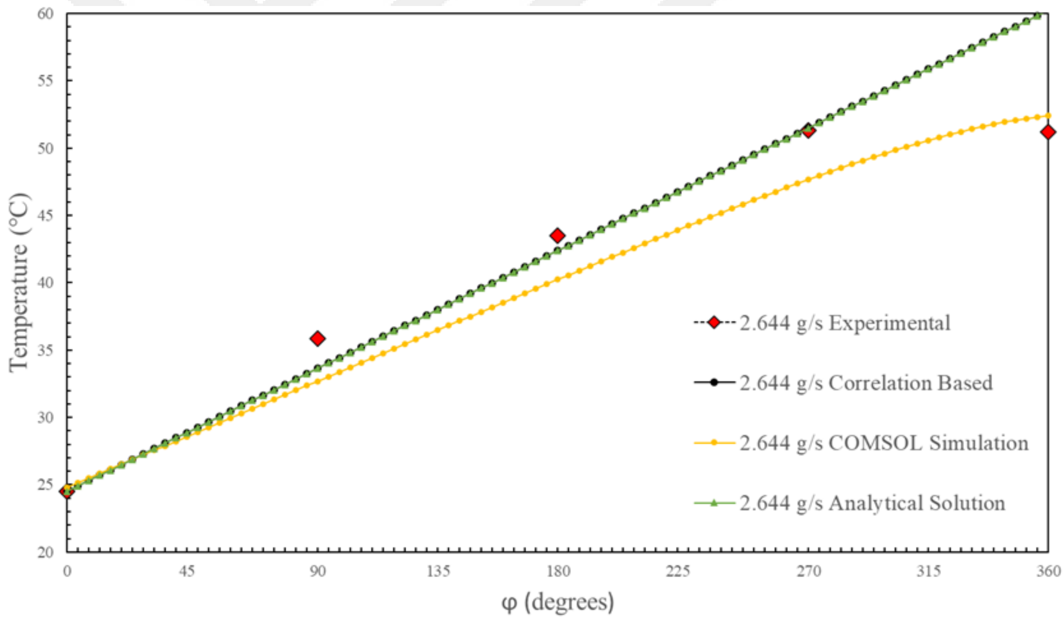

Figure B.6: Temperature distribution comparison along channel between all applied methods and experimental data for 2.644 g/s flow rate

CURRICULUM VITAE

Name Surname : **Ali AMIRFARIDI**

Place and Date of Birth :

E-Mail :

EDUCATION :

PROFESSIONAL EXPERIENCE AND REWARDS: